

Precipitation Strengthening of Aluminum by Transition Metal Aluminides

by

Yangyang Fan

A thesis submitted to the faculty of the

WORCESTER POLYTECHNIC INSTITUTE

in partial fulfillment of the requirements of the degree of

Master of Science

in

Materials Science and Engineering

April, 2012

Professor Makhlof M. Makhlof, Advisor

Professor Richard D. Sisson Jr., Director of the Material Science and Engineering
Program

ABSTRACT

Aluminum-zirconium alloys exhibit superior strength at elevated temperature in comparison to traditional aluminum casting alloys. These alloys are heat-treatable and their strength depends to a large extent on the quenching and aging steps of the heat treatment process. However, measurements show that the critical cooling rate necessary to retain 0.6 wt. pct. zirconium (the minimum amount necessary for significant strengthening) in a super-saturated solid solution with aluminum is 90°C/s, which is un-attainable with traditional casting processes. On the other hand, the critical cooling rate necessary to retain 0.4 wt. pct vanadium and 0.1 wt. pct. zirconium in a super-saturated solid solution with aluminum is only 40°C/s; which suggests that substituting vanadium for zirconium significantly decreases the critical cooling rate of the alloy. This is an important finding as it means that, unlike the Al-0.6Zr alloy, the Al-0.4V-0.1Zr alloy may be processed into useful components by traditional high pressure die-casting. Moreover, measurements show that the hardness of the Al-0.4V-0.1Zr alloy increases upon aging at 400°C and does not degrade even after holding the alloy at 300°C for 100 hours. Also, measurements of the tensile yield strength of the Al-0.4V-0.1Zr alloy at 300°C show that it is about 3 times higher than that of pure aluminum. This increase in hardness and strength is attributed to precipitation of $Al_3(Zr,V)$ particles. Examination of these particles with high resolution transmission electron microscopy (HRTEM) and conventional TEM show that vanadium co-precipitates with zirconium and aluminum and forms spherical particles that have the $L1_2$ crystal structure. It also shows that the crystallographic misfit between the precipitate particles and the aluminum matrix is almost eliminated by introducing vanadium into the Al_3Zr precipitate and that the mean radius of the $Al_3(Zr,V)$ particles is in the range from 1nm to 7nm depending on the alloy composition and aging practice. Finally, it is found that adding small amounts of silicon to the Al-0.4V-0.1Zr alloy effectively accelerates formation of the $Al_3(Zr,V)$ precipitate.

ACKNOWLEDGEMENTS

I have worked with a great number of people whose contribution in various ways to my research and the making of this thesis deserve special mention. It is a pleasure to convey my gratitude to them all in my humble acknowledgement.

I am deeply grateful to Professor Makhlouf M. Makhlouf for giving me the opportunity to work with him on this project. It has been an honor to be his student. I would like to deliver my special gratitude to him for his advice, time, ideas and supervision from the very beginning to the end of this research, as well as for sharing his unique experience with me throughout the work. His words of encouragement and motivation came a long way in bringing this work to completion. I would like to thank Professor Sisson for his advice and guidance throughout these years. He has been a great help not only in my academic performance, but also in my personal development. It is my pleasure also to pay tribute to all the WPI faculty and staff.

I deeply appreciate my family, especially my father. He devoted his life to me, and instructing me to be honest, responsible, and rightness by his acting. Collective and individual acknowledgements are also due to colleagues, classmates and friends whose enthusiasm and support in one way or another was helpful and memorable. The group at the Advanced casting Research Center has contributed immensely to my personal and professional experience at WPI. The team has been a wonderful source of friendships, good advice and collaboration.

I want to thank the Metals Processing Institute and the Department of Materials Science and Engineering at WPI who gave me the opportunity to be a part of them. Finally, I thank everyone who supported and believed in me, and I express my apology to anyone who I did not mention personally.

Table of Contents

ABSTRACT	i
ACKNOWLEDGEMENTS	ii
Table of Contents	iii
1. Objectives	1
2. Background	2
2.1 Precipitation Strengthening.....	2
2.2 The Stability of Precipitates.....	8
2.3 Characteristics of Precipitates in High Temperature Aluminum Alloys.....	10
2.4 Transition Metals that Form Aluminides with Meta-stable $L1_2$ Structure.....	12
2.5 Stable and Meta-stable Crystal Structures of Transition Metal Aluminides.....	14
2.6 Alloying Zirconium Trialuminide (Al_3Zr) with Other Transition Metals.....	16
2.7 Manufacturing Issues.....	17
2.8 The Al-Zr System.....	19
2.9 The Al-V and Al-Zr-V Systems.....	20
2.10 Effect of Silicon and Iron on Precipitation of Transition Metal Aluminides in Aluminum.....	24
3. Apparatuses and Procedures	25
3.1 Design of the Mold used in Measuring the Critical Cooling Rate.....	25
3.2 Design of the Mold used in Measuring Tensile Properties.....	29
3.3 Melt Preparation, Casting, Heat Treatment, and Microstructure Characterization.....	31
3.3.1 Melt Preparation and Casting.....	31
3.3.2 Establishing the Critical Cooling Rate.....	32
3.3.3 Heat Treatment, Hardness Measurement, and Microstructure Characterization.....	32
3.3.4 Elevated Temperature Tensile Property Measurements.....	33
4. Results and Discussion	35
4.1 The Effect of Cooling Rate on the Volume Percent of the Primary Al_3M Phase.....	35
4.1.1 The Binary Al-Zr System.....	35
4.1.2 The Ternary Al-Zr-V System.....	38
4.2. Isothermal Heat Treatment of Binary Al-Zr and Ternary Al-Zr-V Alloys.....	42
4.2.1 The Binary Al-Zr Alloy.....	42
4.2.2 The Ternary Al-Zr-V Alloys.....	43
4.2.3 Thermal Stability of Al-0.4V-0.1Zr Alloy.....	44
4.3 Morphology and Crystal Structure of The $Al_3(Zr,V)$ Precipitates.....	45
4.4 Elevated Temperature Tensile Properties.....	47
5. Conclusions	49
6. References	50

1. Objectives

The objectives of this project are as follows:

1. To determine the critical cooling rate needed to suppress formation of the equilibrium DO_{23} and DO_{22} precipitates in Al-Zr and Al-Zr-V alloys.
2. To establish the optimum heat treatment schedule for processing Al-Zr and Al-Zr-V alloys.
3. To elucidate the mechanism of precipitation in Al-Zr-V alloys and to characterize the structure and size of the precipitate particles.

2. Background

2.1 Precipitation Strengthening

Alfred Wilm[1] discovered that the strength of an Al 4Cu-0.5Mg-0.5Mn alloy is unexpectedly high after quenching it from 525°C and naturally aging it. However, he did not explain the mechanism responsible for the increased strength because of the limitations of the microscopes available at the time. Several years later, Merica, Waltenberg, and Scott[2] published a paper in which they correctly deduced that the different solubility of Cu, Zn, and Mg-Si in aluminum at 525°C and at room temperature leads to the precipitation of a secondary phase which reinforces the strength of the aluminum alloy. However, the nature of the precipitates remained unclear because they are too small to be directly observed by the optical microscope. This issue was not resolved until the early 1960s when diffuse X-ray[3] and transmission electron microscopy[4] were used to investigate precipitates in metallic alloys and today it is well-known that in the binary Al-Cu system, four precipitates form in sequence. They are: Guinier-Preston (GP) zones, θ'' , θ' , and θ . GP zones form first and can form by aging at room temperature; the others require artificial aging, i.e., aging at elevated temperature. All four precipitates strengthen the alloy as a result of their interaction with moving dislocations. The earliest attempt to explain age hardening on the basis of interactions of particles with dislocations is due to Mott and Nabarro [5] who suggested that strengthening arose from the interaction between dislocations and the internal stresses produced by “miss-fitting” coherent precipitates. Consider the situation where the movement of a dislocation is hindered by a precipitate particle as shown schematically in Fig.1. The tension forces T on the dislocation are balanced by the resisting force F . As F increases, the bowing of the dislocation increases, i.e., the angle θ increases. If the particle is hard, the resisting force F is large and can be larger than $2T$. In this case, the dislocation will bypass the particle either by Orowan looping or by cross-slipping. In this scenario, the particle remains unchanged; however, if the maximum resistance force is attained and $\sin\theta < 1$, then the particle will be sheared by the dislocation as the dislocation passes through it.

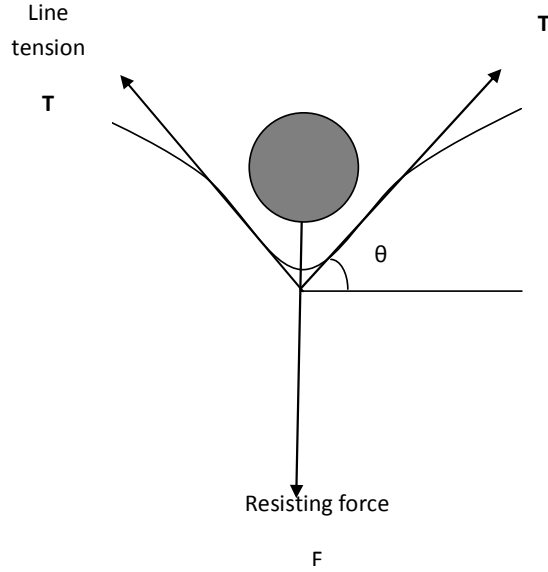


Fig.1. Balance of forces acting on a precipitate particle as a dislocation attempts to pass by it.

Precipitate looping occurs if the precipitate particles are ‘hard’ enough that dislocations pass through them without causing them to deform. Typically, this happens in four steps as depicted schematically in Fig.2. These are: (1) the approach step, (2) the sub-critical step, (3) the critical step, and (4) the escape step. Orowan [6] considered the relationship between the applied stress and dislocation bowing and derived the relationship:

$$\Delta\tau_{or} = Gb/L \quad (1)$$

where $\Delta\tau_{or}$ is the increase in yield stress due to the precipitation looping, G is the shear modulus of the matrix, b is the Burger’s vector of the dislocation, and L is the particle spacing. Ashby[7] further developed this equation by taking into account the inter-particle spacing and the effects of statistically distributed particles. The Ashby-Orowan relationship is given as

$$\Delta\sigma_{ao} = 0.538 \cdot \frac{Gb f^{1/2}}{D} \cdot \ln\left(\frac{D}{2b}\right) \quad (2)$$

In Eq. (2), $\Delta\sigma_{ao}$ is the increase in yield strength, G is the shear modulus of the matrix, b is the magnitude of the Burgers vector, D is the real diameter of the particle, and f is the volume fraction of particles. A plot of the Ashby-Orowan stress as a function of

precipitate diameter for different volume fractions of particles in an aluminum matrix as generated by Eq. (2) with $G = 26.2$ GPa, and $b = 0.286$ nm is shown in Fig.3.

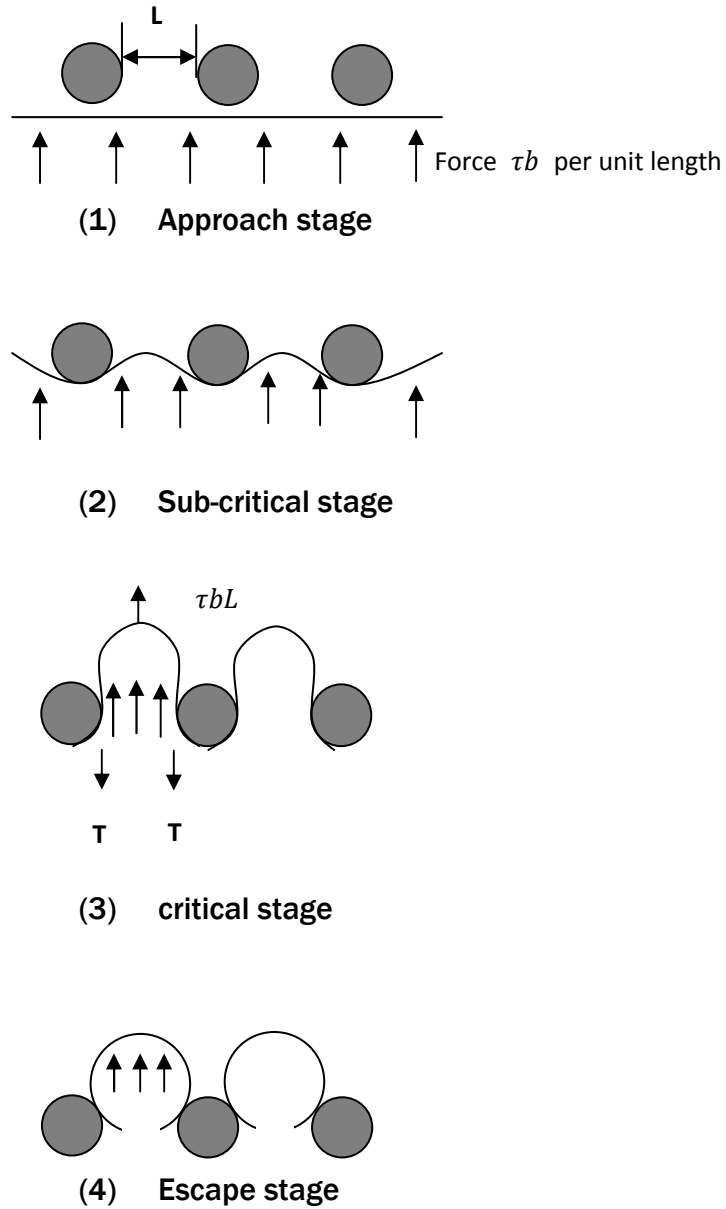


Fig.2. The four steps of precipitation looping.

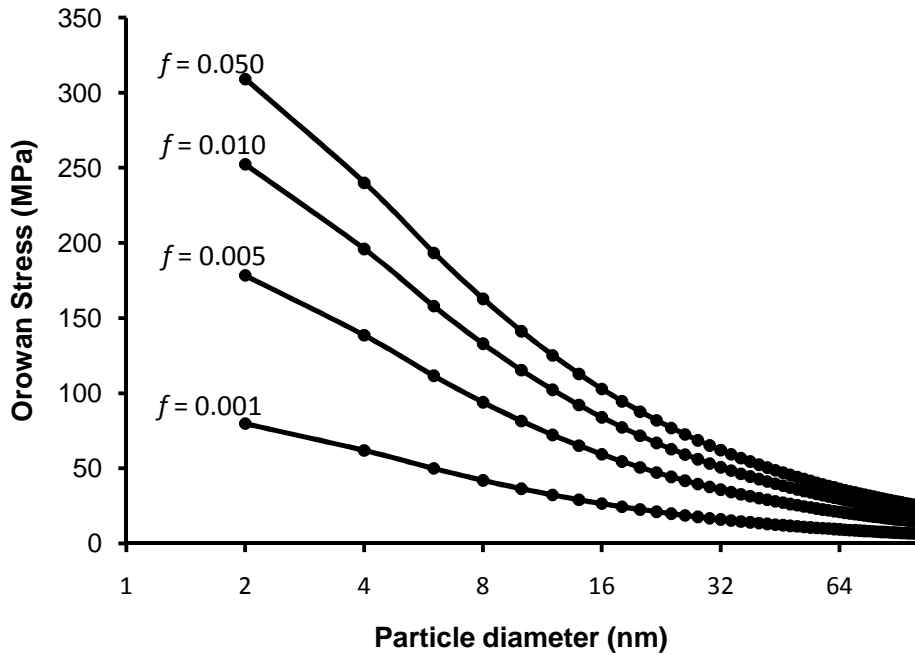


Fig.3. The Ashby-Orowan stress as a function of precipitate diameter for various precipitate volume fractions, f .

The dislocation loops the precipitate particle when the particle is hard, but what really impedes the movement of the dislocation is the strain field around the miss-fitting coherent precipitate. Mott and Nabarro[8] described phenomenon. Briefly, coherent strain fields around the precipitate cause repulsive forces against the dislocation as shown schematically in Fig.4. Consequently, the dislocation is stopped by the restraining force at the edge of the coherent precipitate. As the restraining force increases, the convolutions of the dislocation increase up to the point where Orowan looping occurs.

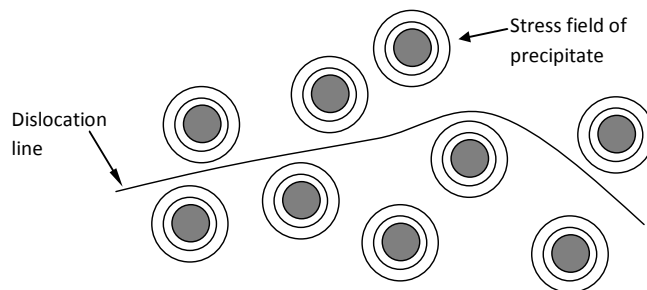


Fig.4. Interaction between a dislocation and precipitate particles.

When the precipitates are relatively small, dislocation bending is limited; and the shear stress $\Delta\tau$ from the strain field is given by

$$\Delta\tau = 4G\varepsilon^2\left(\frac{rf}{b}\right)^{1/2} \quad (3)$$

In the case of relatively larger precipitates, where considerable flexing of the dislocations occurs as a result of the large spacing between the individual precipitate particles, any movement of the dislocation will have to overcome a larger number of obstacles per unit length and the shear stress $\Delta\tau$ is given by

$$\Delta\tau = 0.7Gf^{1/2}\varepsilon^{1/4}\left(\frac{b}{r}\right)^{3/4} \quad (4)$$

In both Eq.(3) and Eq.(4), the misfit strain ε is defined as:

$$\varepsilon = |\delta| \left[1 + \frac{2G_p(1-2\nu_p)}{G_p(1+\nu_p)} \right] \quad (5)$$

Where G_p is shear modulus of the precipitate, ν_p is Poisson's ratio of the precipitate, and δ is related to the difference between the lattice parameters of the precipitate (α_p) and the matrix (α)

$$\delta = \frac{\alpha_p - \alpha}{\alpha} \quad (6)$$

Fig. 5 shows the relationship between shear strength and the average size of the precipitate for small and large precipitates. For this plot, the shear modulus of the Al_3Zr particles is $G_p = 196 \text{ GPa}$, and its misfit strain in aluminum is $\varepsilon = 7.67 \times 10^{-3}$ [9]. Fig. 5 shows that for small particles, coherency strain hardening increases with increased particle size, whereas for larger particles, it decreases with increased particle size, giving rise to a maximum strengthening effect at a critical particle size which is of the order of

$$r = \frac{b}{4\varepsilon} \quad (7)$$

As pointed out previously, the upper limit of this form of strengthening is imposed by the transition to the classical Orowan looping process.

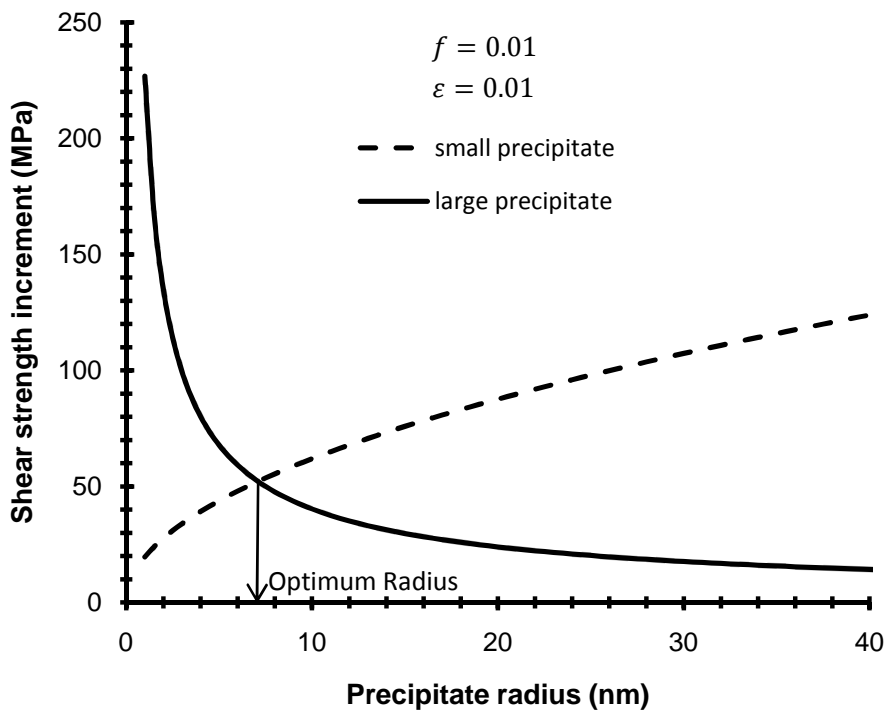


Fig.5. Shear strength increment due to coherent strengthening

When dislocations penetrate the precipitate, the precipitate will be deformed, as shown schematically in Fig.6. In this case, there are several factors that may be involved in raising the stress level required for plastic yielding. These include:

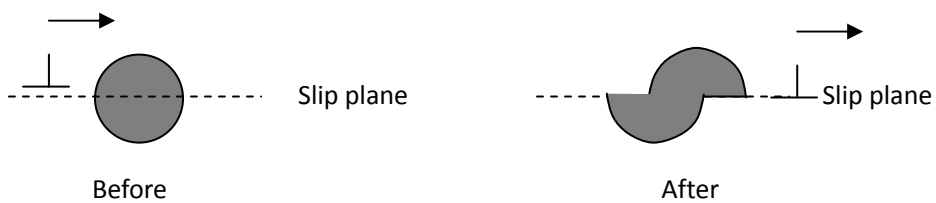


Fig.6. A precipitate particle being cut by a dislocation.

(1) **Chemical Strengthening** –the passage of the dislocation through the precipitate creates two ledges of new precipitate-matrix interface of specific energy γ_s . The shear strength increment due to Chemical Strengthening is given by

$$\tau_c = \left(6 \frac{\gamma_s^3 b f}{\pi \Gamma}\right)^{1/2} \langle r \rangle^{-1} \quad (8)$$

Where γ_s is energy of a matrix-precipitate interface created by slip, $\langle r \rangle$ is the average radius of the precipitate particles, and Γ is the line tension of a dislocation. Eq. (8) shows that the smaller the average precipitate radius, the more the Chemical Strengthening. Chemical Strengthening is usually a minor contributor to precipitation hardening, and it is not as important as Stacking-Fault Strengthening.

(2) Stacking-fault Strengthening - the passage of the dislocation through the precipitate produces a stacking fault within the precipitate. Because the stacking fault energy and width in precipitates are different from their counterparts in the matrix, the movement of the dislocation is impeded by the precipitate. According to Hirsch and Kelly[10] and Gerold and Hartmann[11] the maximum force experienced by the split dislocation is given by

$$F_m = \Delta\gamma l \quad (9)$$

Where $\Delta\gamma$ is the difference between the stacking fault energy in the matrix and in the precipitate, l is the length of the chord inside the precipitate at the critical breaking condition depicted in Fig. 7. The shear strength increment due to Stacking-Fault Strengthening is given by

$$\tau_{c\gamma} = \Delta\gamma^{\frac{3}{2}} \left(\frac{3\pi^2 f \langle r \rangle}{32\Gamma b^2}\right)^{1/2} \quad (10)$$

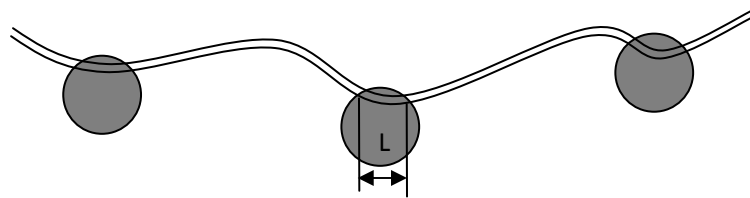


Fig.7. Dislocation-precipitate interactions in stacking-fault strengthening.

2.2 The Stability of Precipitates

When an alloy is employed at an elevated temperature, Ostwald ripening of the

precipitate particles may occur; i.e., the larger precipitate particles may grow even larger at the expense of the small precipitate particles. As a consequence, the average radius of the precipitate particles increases at elevated temperatures while the density of the particles decreases. As pointed out earlier, precipitation hardening strongly depends on the average radius of precipitate. Large, coarsened precipitates contribute little to precipitation hardening.

The kinetics of Ostwald ripening is controlled by volume diffusion, as solute atoms are transferred through the matrix from the shrinking precipitates to the growing ones. Lifshits, Slyozov [12] and Wagner [13] (the LSW theory) shows that the average precipitate size $\langle r \rangle$ increases with time t according to

$$(\langle r(t) \rangle)^3 - (\langle r(t=0) \rangle)^3 = kt \quad (11)$$

where $\langle r(t) \rangle$ is the average precipitate radius at time t , $\langle r(t=0) \rangle$ is the average precipitate radius at the onset of coarsening, and k is a rate constant given by Eq. (12) in which D is the diffusivity of the rate-controlling solute, σ is the precipitate-matrix interfacial free energy, and C_e^p and C_e^m are the equilibrium solubilities of the solute elements in the precipitate and matrix phases, respectively.

$$k \propto \frac{D\sigma}{(C_e^p - C_e^m)^2} \quad (12)$$

For creep-resistant alloys, the Ostwald ripening process must be slowed down. Hence, it is essential to have in the alloy solutes with low diffusion coefficient and low solubility in the matrix, and that form precipitates with a low interfacial energy with the matrix.

In order to illustrate this point, consider the three aluminum alloys:

- (1) Al-Si12-Cu-Mg-Ni (eutectic composition),
- (2) Al-Si18-Cu-Mg-Ni (hypereutectic composition), and
- (3) Al-Si12-Cu4-Ni-Mg (special eutectic alloy).

Their yield strength and fatigue strength diminish rapidly with increased temperature due to coarsening and dissolution of their precipitated phases, as depicted in Table 1 [14]. The major strengthening phases in the eutectic and hypereutectic alloys are

β' -Mg₂Si and θ' -Al₂Cu precipitates. When the temperature is above 200°C, precipitate coarsening becomes significant and as a consequence, the β' -Mg₂Si and θ' -Al₂Cu precipitates evolve into incoherent β -Mg₂Si and θ -Al₂Cu precipitates, respectively. The loss of coherency between the matrix and the precipitate further accelerates the coarsening process until eventually the coarsened low-density precipitates totally lose their strength.

Table 1. Effect of temperature on the yield and fatigue strength of aluminum alloys.

	Eutectic Alloy Al-Si12-Cu-M-gNi		Hypereutectic Alloy Al-Si-18-Cu-Mg-Ni		Special Eutectic alloy Al-Si12-Cu4-NiMg
	Cast	Forged	Cast	Forged	Cast
<u>Yield Strength (in MPa) at Temperature:</u>					
20°C	190-230	280-310	170-200	220-280	200-280
150°C	170-220	230-280	150-190	200-250	-----
200°C	120-170	-----	100-150	-----	150-200
250°C	80-100	90-120	80-120	100-140	100-150
300°C	50-80	-----	60-80	-----	85-100
<u>Fatigue strength (in N/mm²) at Temperature:</u>					
20°C	80-120	110-140	80-110	90-120	90-120
150°C	70-110	90-120	60-90	70-100	90-120
250°C	50-70	60-70	40-60	50-70	60-80
300°C	-----	-----	-----	-----	45-60

2.3 Characteristics of Precipitates in High Temperature Aluminum Alloys

Several precipitate characteristics must be considered when designing aluminum alloys for high temperature applications. These include: (1) overall thermal stability, (2) volume fraction, (3) average radius, and (4) coherency with the matrix.

First, as mentioned earlier, the different solubility of elements in the α -Al matrix at high temperature and at low temperature is the reason for second phase precipitation. The maximum solubility C_{max} , and the slope of the solvus line k , are the two most important parameters, as shown in Fig.8. They determine whether or not the alloy will precipitate a large amount of globally distributed fine phases. Even though for some types of age-hardenable alloys, the maximum solubility C_{max} is small, (e.g., the maximum

equilibrium solubility of scandium and zirconium in aluminum is only 0.28 at.%[15] and 0.083 at.%[16], respectively) they still yield excellent precipitation strengthening by means of proper heat treatment because the slope of the solvus line k for the alloy is very steep.

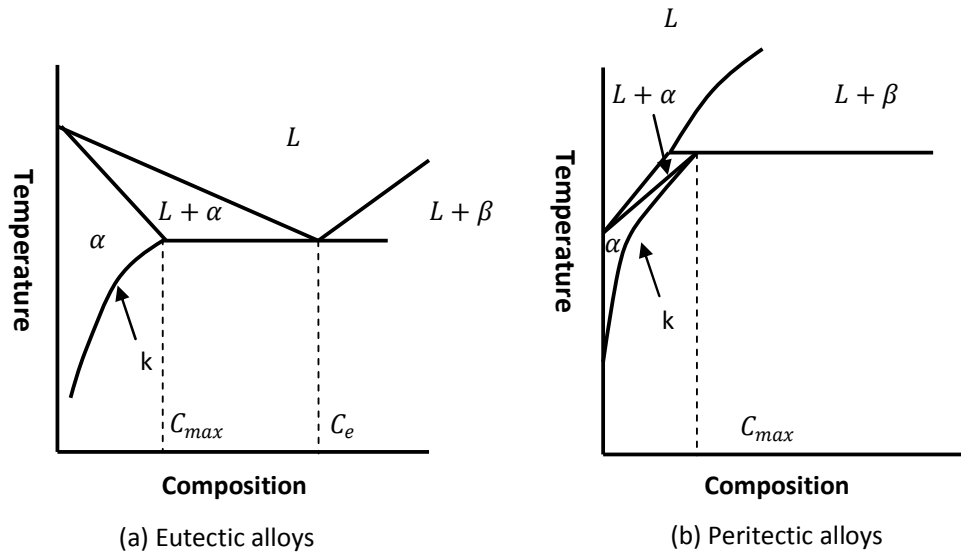


Fig.8. The maximum solubility and solvus line in (a) eutectic alloys and in (b) peritectic alloys.

Second, the average size of the precipitates strongly influences the yield strength of the alloy. For the precipitate looping, stacking-fault, and Chemical Strengthening mechanisms, the smaller the precipitate, the higher the yield strength of the alloy. However, there is an optimum radius for the coherent strengthening mechanism where strengthening is maximized.

Third, Fine [17] suggested that when the precipitate is coherent and coplanar with the matrix, dislocations in the matrix can readily traverse through the precipitate particles, and if the precipitate and matrix have different structures, then the dislocations which traverse the precipitate create stacking faults in the precipitate. Since a large amount of energy is required to create the stacking fault and the traversing dislocation creates more stacking fault with each unit of slip, this is a very effective strengthening mechanism for elevated temperatures. Also, the coherent-coplanar correspondence between the precipitate and matrix means that the precipitate-matrix interface is a low

energy interface and there is little tendency for coarsening or coalescence of the precipitate particles. Therefore, good coherency between the precipitate particles and the matrix is favored for precipitation strengthening.

Fourth, low diffusivity of the solute elements in the matrix effectively minimizes the coarsening of the precipitate particles at high temperature.

2.4 Transition Metals that Form Aluminides with Meta-stable L1₂ Structure

Addition of transition elements to aluminum can result in the formation of a large density of elastically stiff Al₃M (M ≡ transitional element) precipitates. The Al₃M precipitates with L1₂ structure are fully coherent with the aluminum matrix and therefore they can considerably strengthen the alloy. Table 2 shows the maximum solubility (C_{max}) and the solubility at 400°C ($C_{400^\circ C}$) for some transition metals in aluminum.

Table 2. Solubility of some transition metals in aluminum.

Element	C_{max} (at.%)	$C_{400^\circ C}$ (at.%)	$\frac{C_{max}}{C_{400^\circ C}}$	Reference
Group 3 transition elements				
Sc	0.23	0.01	23.0	[18,19]
Y	0.049	0.016	3.1	[18,20]
Group 4 transition elements				
Ti	0.15	0.03	5	[21]
Zr	0.083	<0.025	166	[22]
Hf	0.186	0.13	1.4	[18,23]
Group 5 transition elements				
V	0.33	<0.15	2.2	[18]
Nb	0.066	0.038	1.7	[18]
Ta	0.235	0.05	4.7	[18]

Because nearly all the Al₃M particles precipitate at around 400°C, the ratio C_{max} to $C_{400^\circ C}$ is a good indicator of the tendency of the alloy to form precipitates with the L1₂ structure. A larger ratio indicates that more precipitates will form after solutionizing and

aging. As Table 2 indicates, zirconium and scandium are superior to the other transition metals in that respect; accordingly they have been comprehensively studied [35]-[52]. However, the high cost of scandium limits its application and the mechanical properties of Al-Zr alloys are far below what is expected.

The diffusivity of transition metals in aluminum directly influences the thermal stability of the Al₃M precipitates. As Table 3 shows, the diffusion coefficients of the various transition metals in aluminum at 400°C are at least three magnitudes smaller than that of copper (2.27×10^{-14} m/s)[29] or Mg (6.14×10^{-14} m/s)[30] in aluminum. Therefore, Al₃M precipitates are more thermally stable than traditional precipitation hardening phases, such as θ' -Al₂Cu and β' -Mg₂Si.

Table 3. Diffusion coefficients of some transition metals in aluminum.

Element	D_0 m ² s ⁻¹	Q kJmol ⁻¹	D at 400°C m ² s ⁻¹	Reference
Sc	5.31×10^{-4}	124	1.98×10^{-17}	[24]
Ti	1.12×10^{-1}	260	7.39×10^{-22}	[25]
V	1.60	303	4.85×10^{-24}	[24]
Zr	7.28×10^{-2}	242	1.20×10^{-20}	[25]
Hf	1.07×10^{-2}	242	2.11×10^{-21}	[26]
Cr	10.00	282	1.29×10^{-21}	[27]
Fe	7.7×10^{-1}	221	5.14×10^{-18}	[28]

Coherency determines the strengthening mechanisms and the thermal stability of precipitates. Lower misfit with the aluminum matrix not only leads to better thermal stability of the precipitate, but it also results in higher yield strength at high temperature. Table 4 shows the mismatch of some Al₃M precipitates with aluminum. All the phases are metastable and have the L1₂ structure. As Table 4 shows, Sc, Y, Zr, and Nb trialuminides have a positive mismatch with aluminum; while Ti, Hf, and V trialuminides have a negative mismatch. A possible way to decrease the misfit between the precipitate and the matrix is to alloy the L1₂ precipitates. Some alloying elements may change the lattice parameter of the L1₂ precipitate and by a proper heat treatment

the mismatch between the precipitate and the matrix may be considerably reduced or even eliminated.

Table 4. Magnitude of the mismatch between transition metal trialuminides and aluminum.

Trialuminide	Lattice parameter (nm)	Mismatch with Al	Absolute mismatch Δ	Reference
Group 3 transition elements				
Al ₃ Sc	0.4103	+1.32%	1.32%	[27]
Al ₃ Y	0.4234	+4.55%	4.55%	[23]
Group 4 transition elements				
Al ₃ Ti	0.4048	-2.04%	2.04%	[53]
Al ₃ Zr	0.4080	+0.75%	0.75%	[53-55]
Al ₃ Hf	0.4048	-0.04%	0.04%	[53]
Group 5 transition elements				
Al ₃ V	0.3870	-4.44%	4.44%	[56]
Al ₃ Nb	0.4110	+1.49%	1.49%	[57]

2.5 Stable and Meta-stable Crystal Structures of Transition Metal Aluminides

Many transition metal trialuminides form with the meta-stable L1₂ structure when the alloy isothermally aged from the supersaturated solid solution. These fine L1₂ precipitates not only yield excellent strength, but also they are thermally stable because they are fully coherent with the matrix. However, if they are over-aged, or if they are aged at a higher than optimum temperature, they will transform to the complex tetragonal DO₂₂ or DO₂₃ structure (see Fig. 9). The DO₂₂ and DO₂₃ precipitates are semi-coherent with the aluminum matrix. As a result, the coherency strengthening of the alloy will diminish when these precipitates form at the expense of the L1₂ precipitates. And most importantly, the loss of coherency between the precipitate and the matrix accelerates Ostwald Ripening of the precipitate; as a consequence, the alloy will lose nearly all its precipitation strengthening effect.

When the transition metal trialuminide precipitates are aged at a temperature that is higher than a critical temperature, they will quickly transform from the meta-stable L1₂

structure to the complex tetragonal structure. As may be seen in Table 5, different transition metal trialuminides have different critical conversion temperatures because of their different Gibbs free energy, diffusivity, and coherency energy. The transition metal trialuminide that has the higher conversion temperature is the more thermally stable one; therefore the conversion temperature is the upper-limit of the aging temperature. Table 5 shows that $\text{Al}_3\text{V}_{0.875}\text{Zr}_{0.15}$ has the highest conversion temperature while Al_3Sc has the lowest. There are two reasons for this: first, the diffusivity of vanadium in the aluminum matrix is the lowest among all the transition metals while that of scandium is the highest (see Table 3) and second, the misfit between Al_3Sc and aluminum is relatively large while the misfit between $\text{Al}_3\text{V}_{0.875}\text{Zr}_{0.15}$ and aluminum is nearly zero[37] (see Table 4).

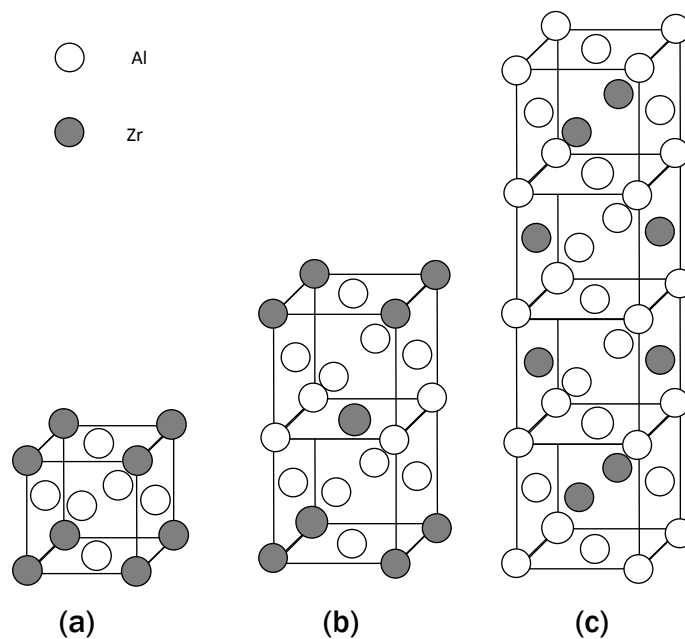


Fig.9.(a) The L1_2 crystal structure,(b) The D0_{22} crystal structure and (c) The D0_{23} Crystal structure.

Table 5. Conversion temperature and stable structure of transition metal trialuminides.

Phase	Meta-stable structure	Conversion temperature	Stable structure	Reference
Al_3Sc	$L1_2$	350°C	26 facets $L1_2$	[33]
Al_3Zr	$L1_2$	>500°C	Fan or rod shape DO_{23}	[32] [34]
$\text{Al}_3\text{Sc}_{0.6}\text{Zr}_{0.4}$	$L1_2$	500°C	Rod shape DO_{23}	[35]
$\text{Al}_3\text{V}_{0.875}\text{Zr}_{0.15}$	$L1_2$	600°C	Rod shape DO_{23}	[33]

2.6 Alloying Zirconium Trialuminide (Al_3Zr) with Other Transition Metals

As mentioned earlier, aluminum alloys that contain Al_3Sc and Al_3Zr are among the most promising alloys for high temperature applications; and therefore a large number of studies have been devoted to investigating the potential of alloying the Al_3Zr and Al_3Sc precipitates in these alloys with other transition elements while retaining the $L1_2$ structure. Some of these studies are listed in Table 6.

Basically, there are three motivations behind alloying Al_3Zr and Al_3Sc with other transition metals. These are; (1) Al_3Sc has excellent properties at high temperature; however, it is too expensive. Therefore, substituting Sc with another element may decrease the cost of the alloy [35-42]. (2) The misfit between the precipitate and the matrix is an important parameter in precipitation hardening. Therefore, some researchers [37] tried to alloy the Al_3Zr and Al_3Sc precipitates with other transition metal(s) in order to decrease the misfit, and thus increase the thermal stability of the precipitate. Others [44, 49] believed that a larger coherent misfit can enhance the creep resistance of the alloy and so they tried to increase the misfit by alloying the precipitate. (3) In Ostwald Ripening the large precipitates grow even larger at the expense of the smaller precipitates. Researchers at U.C. Berkeley successfully made the size of the Al_3Sc precipitates uniform by alloying the precipitate with Li and Zr, and thus they managed to improve the thermal stability of the alloy [43].

Among all these alloyed Al_3M precipitates, $\text{Al}_3\text{Zr}_x\text{V}_{1-x}$ is the most interesting, mainly

because of the low diffusivity of vanadium in aluminum, and the low misfit between $\text{Al}_3\text{Zr}_x\text{V}_{1-x}$ particles and aluminum, which make alloys that contain these precipitates thermally stable. Moreover, vanadium can substitute for a large fraction of the zirconium (as high as 87.5%); and the liquidus temperature of the vanadium-aluminum system is considerably lower than that of other transition metal-aluminum systems.

Table 6. Alloying elements in Al_3Sc and Al_3Zr trialuminides.

Trialuminide	Alloying elements	Reference	
Al_3Sc	Zr	[35–42]	
	Si	[47]	
	La elements	Tb	[48]
		Ho	[48]
		Tm	[48]
		Lu	[48]
		Gd	[44]
		Yb	[44]
	Li, Zr	[43]	
Zr, Hf	[46]		
Al_3Zr	V	[33, 51, 51]	
	Ti	[45, 50]	
	Er	[49]	
	Sc	[35–42]	
	Sc, Hf	[46]	

2.7 Manufacturing Issues

The equilibrium form of the majority of the transition metal trialuminides forms by a peritectic reaction and the precipitate that forms is often coarse, incoherent with the aluminum matrix, and adds little strength to the alloy. Thus, formation of the

equilibrium trialuminides must be suppressed. The most effective and practical way to suppress formation of the equilibrium trialuminides is to quench the melt from the holding temperature at a fast enough cooling rate so as to prevent nucleation and growth of the stable trialuminides and end up with a super-saturated solid solution of the transition metals in α -aluminum. In essence, it is necessary to eliminate the homogenization step of the typical precipitation hardening heat treatment.

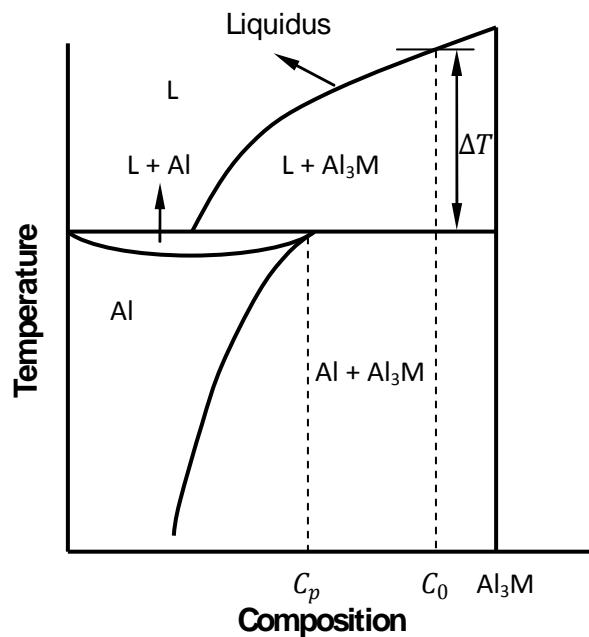


Fig. 10.The Al-rich corner of a typical Al-M (M=transition metal) phase diagram.

Fig. 10 shows the Al-rich corner of a typical Al-M (M = transition metal) phase diagram. The liquidus line of the Al_3M phase is quite steep, which makes attempts to suppress formation of the stable Al_3M almost impossible. The energy barrier to forming the equilibrium Al_3M phase ($\Delta G_{Al_3M}^*$) is related to the under-cooling of the melt (ΔT) by [58]

$$\Delta G_{Al_3M}^* = \frac{c}{\Delta T^2} \quad (13)$$

As Fig.10 shows, for a melt with concentration C_0 (where $C_0 > C_p$) that is quenched into the (L + Al_3M) region of the phase diagram, the under-cooling (ΔT) is quite large, and hence the energy barrier to nucleation of the Al_3M phase ($\Delta G_{Al_3M}^*$) is small. The

Volmer-Weber theory [58] relates the homogenous nucleation rate (I) of the Al_3M phase to the energy barrier to nucleation, $\Delta G_{Al_3M}^*$

$$I = AT \exp\left(-\frac{\Delta G_a}{N_A k_B T}\right) \exp\left(-\frac{\Delta G_{Al_3M}^*}{N_A k_B T}\right) \quad (14)$$

where k_B is the Boltzmann constant, and ΔG_a is the free energy of activation for the short-range diffusion of a mole of atoms or molecules moving a fraction of an atomic distance across an interface to join a new lattice. Fig. 11 shows the process of nucleation of the Al_3M phase during continuous cooling based on Eq. (14). The change in the number of Al_3M nuclei with time follows an S-shape curve, and when $t < t^*$, the number of nuclei is almost zero. Therefore, there is a critical cooling rate at which nucleation of the equilibrium Al_3M phase could be avoided.

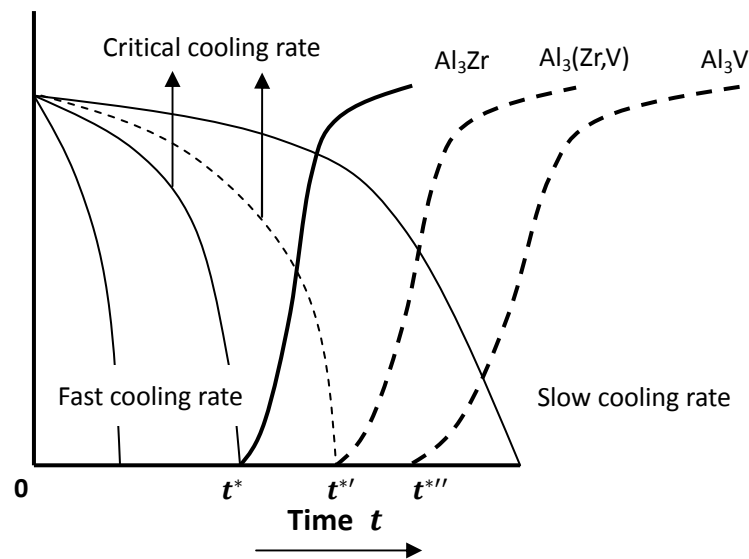


Fig.11. Schematic representation of the nucleation of the Al_3M phase from the melt.

2.8 The Al-Zr System

Fig.12 shows the Al-rich corner of the Al-Zr phase diagram [22]. The maximum solubility of Zr in α -Al is 0.08 at % (0.28 wt %) at 667°C, but even if all that zirconium is dissolved into α -Al at 667°C, only about 0.3% volume fraction of Al_3Zr particles will precipitate after aging. According to the Ashby-Orowan theory, such a small amount contributes

insignificantly to precipitation hardening the alloy.

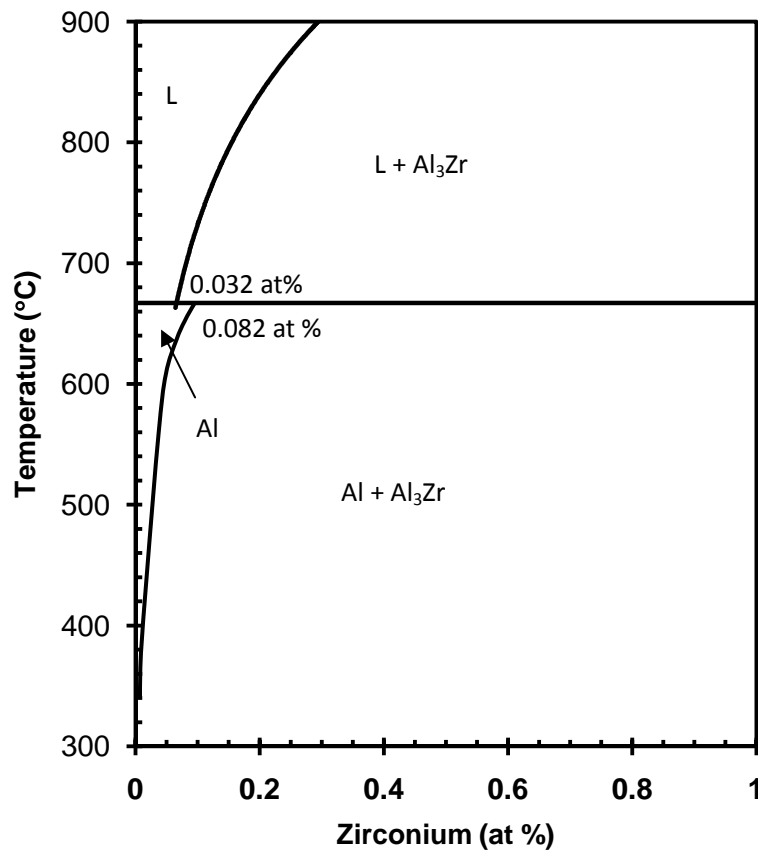


Fig.12. The Al rich corner of the aluminum-zirconium phase diagram.

However, if the Al-Zr alloy is quenched very fast, the solubility of zirconium in α -Al could be doubled. Ryum [59] solutionized 0.5 wt% zirconium into α -Al by quenching the melt into a copper chilled mold. Similarly, Knipling [60] quenched a small amount (7 g) Al-0.65Zr into a chilled crucible that produced a cooling rate of 10-100°C/s and obtained a supersaturated solid solution. Upon aging at 375°C for 24 hrs, the precipitate that formed added about 500MPa to the strength of the alloy. However, if the amount of zirconium exceeds 0.8 wt%, the primary Al₃Zr phase cannot be suppressed by conventional quenching processes. [61]

2.9 The Al-V and Al-Zr-V Systems

Comparison of Fig. 12 to Fig. 13 shows that the curvature of the liquidus line of the Al-V system is gentler than that of the Al-Zr system; and at 800°C, aluminum can dissolve

only 0.2 at.% zirconium while as much as 0.4 at.% vanadium can be dissolved at this temperature. Moreover, for the same amount of zirconium and vanadium dissolved in separate aluminum melts, the critical cooling rate needed to suppress the formation of primary Al_3V is significantly slower than that needed to suppress the formation of primary Al_3Zr . Hence, if zirconium is substituted by vanadium to form the mixed transition metal aluminide $\text{Al}_3(\text{Zr},\text{V})$, then the critical cooling rate to suppress the formation of $\text{Al}_3(\text{Zr},\text{V})$ primary phase would be between that needed to suppress the formation of primary Al_3V and primary Al_3Zr .

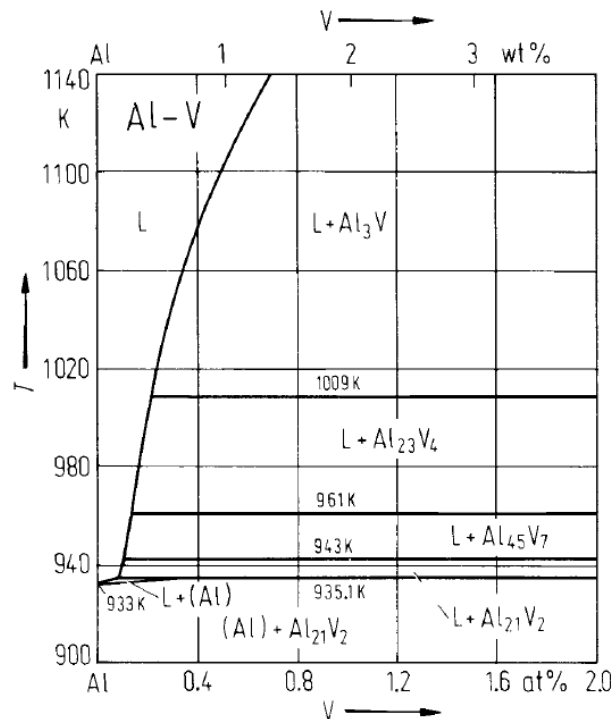


Fig.13. The Al rich corner of the aluminum-vanadium phase diagram.

Zedalis [37] cast an Al-0.4V-0.1Zr (wt%) alloy in a copper mold and used Select Area Diffraction to show that vanadium substituted for 85 at.% of zirconium in the L1_2 precipitates that formed after aging. Also Chen [62, 63] cast a variety of high concentration vanadium and zirconium alloys by melt spinning; and precipitated a high concentration of meta-stable L1_2 particles in the alloys by aging at 425°C. Moreover, both Zedalis and Chen showed that the $\text{Al}_3(\text{Zr},\text{V})$ co-precipitate exhibits better thermal

stability than the Al_3Zr precipitate.

The ternary phase diagrams of the Al-Zr-V system aid in producing L1_2 precipitates in this system. Basically, there are two requirements to get L1_2 precipitates:

- (1) All the zirconium and vanadium must be dissolved into the liquid aluminum and form a super-saturated solid solution upon freezing. As Fig. 14 shows, the maximum solubility of vanadium plus zirconium is about 5 at.% at 1100°C , and the ratio of vanadium to zirconium at this point is 2.5. But since the typical pouring temperature for foundry casting is much lower than 1100°C (about 780°C), and since typical cooling rates during foundry casting are slow, then the practical amount of zirconium plus vanadium must be significantly less than 5 at.%
- (2) The tendency to form L1_2 precipitates depends to a large extent on how steep the solvus line of the system is. A steeper solvus line equates to a higher tendency to form a metastable L1_2 precipitate. Fig.15 shows that only trace amounts of zirconium or vanadium dissolve in aluminum at 477°C , and thus the driving force to precipitate metastable particles is high.

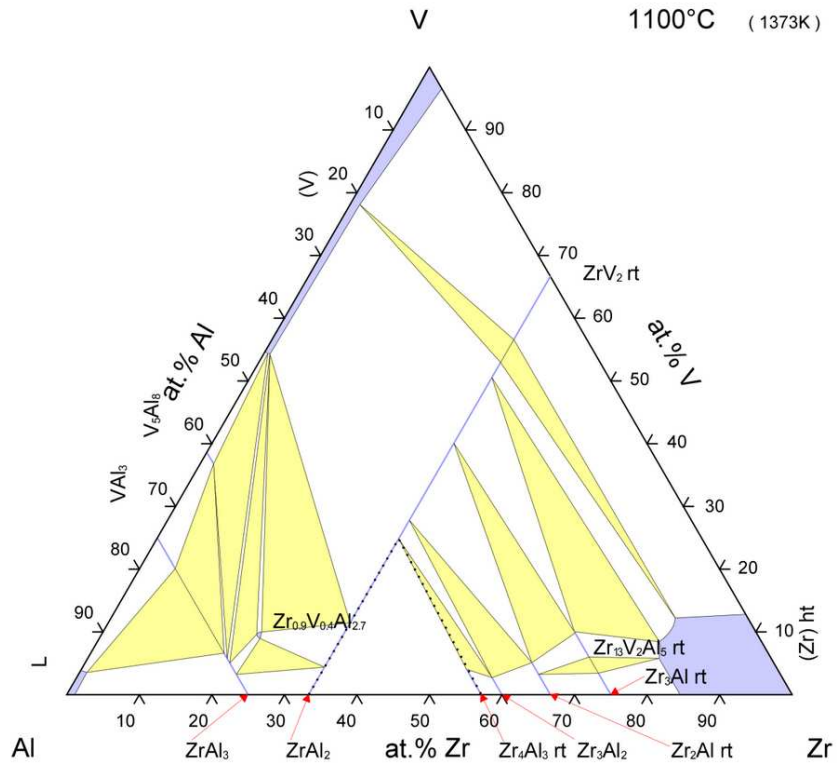


Fig.14. Isothermal ternary phase diagram of the Al-Zr-V system at 1100°C.

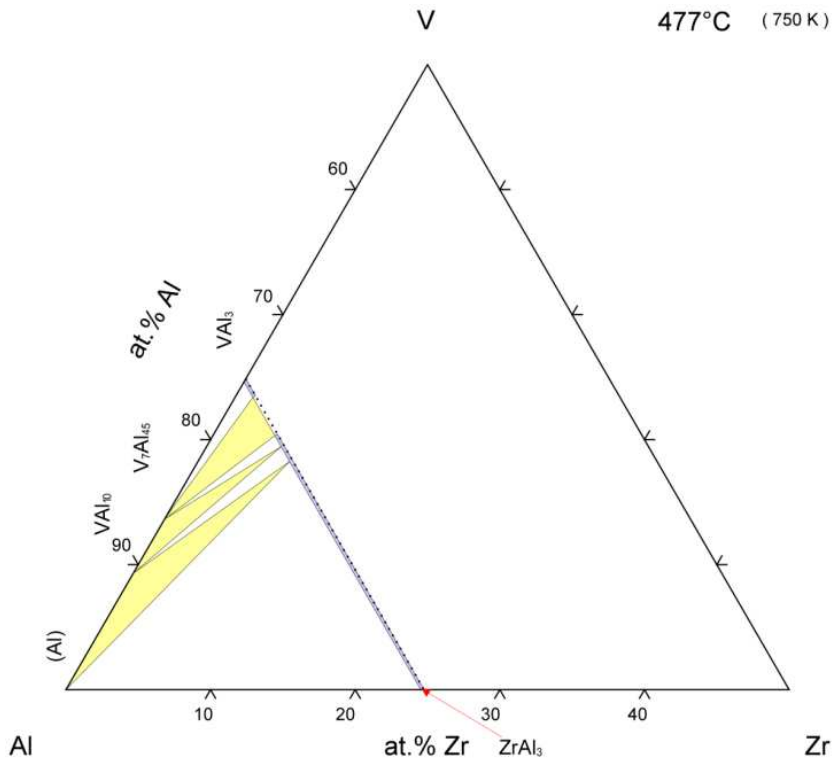


Fig.15. Isothermal ternary phase diagram of the Al-Zr-V at 477°C.

2.10 Effect of Silicon and Iron on Precipitation of Transition Metal Aluminides in Aluminum

Adding silicon and iron to an Al-Zr alloy accelerates the precipitation rate of Al_3Zr [64, 65]. Hori et al. [65] investigated the precipitation behavior of Al_3Zr with transmission electron microscopy (TEM) and with resistivity measurements and concluded that silicon provides nucleation sites for the continuous precipitation of Al_3Zr . Takeshi [65] suggested that adding iron to an Al-Zr alloy slightly accelerates the precipitation of Al_3Zr , while adding silicon more significantly accelerates it. The most significant effect occurs at temperatures 50-100K below the temperature at which the maximum amount of zirconium precipitates in the Al-Zr-Fe and Al-Zr-Si alloys.

3. Apparatuses and Procedures

3.1 Design of the Mold used in Measuring the Critical Cooling Rate

The driving force to precipitate primary transition metal aluminides in aluminum is quite large[54]. Therefore, a very high cooling rate is necessary in order to suppress their nucleation. In order to quantify the critical cooling rate necessary to suppress the formation of primary Al_3Zr and $Al_3(Zr,V)$ in Al-Zr, Al-Zr-V alloys, a mold was designed and manufactured to quench the alloys at various cooling rates. The mold was designed to meet two requirements:(1)It provides a cooling rate gradient along the length of the mold; and (2) the fastest cooling rate is about $100^\circ C/s$, which is in the range of cooling rates typical of high pressure die casting aluminum alloys. In order to meet these requirements, the cone-shaped mold shown schematically in Fig.16 was designed. The total capacity of the mold is 200 cm^3 , which corresponds to about 540 grams of aluminum. The mold was machined from brass because brass has high thermal conductivity and good machinability. During casting, the mold is immersed in room temperature water(up to its rim) in order to further enhance heat extraction from the solidifying metal. The solidification simulation software MAGMASOFT[®] was used to simulate the solidification process in the mold. As shown in Fig.17 the melt begins to solidify at the bottom of the mold and solidification progresses towards the top. The results of the simulation also show that the cooling rate¹ ranges along the central axis of the ingot from $114^\circ C/s$ at the bottom to about $20^\circ C/s$ at the top, which prove that the mold meets the requirements.

¹The cooling rate (δ) is defined as the average cooling rate between $800^\circ C$ and the temperature at the end of solidification, T_{end} so that

$$\delta = \frac{800^\circ C - T_{end}^\circ C}{\tau} \quad (15)$$

In Eq. (15) T_{end} can be identified from temperature - time curves and τ is the time between $800^\circ C$ and T_{end} .

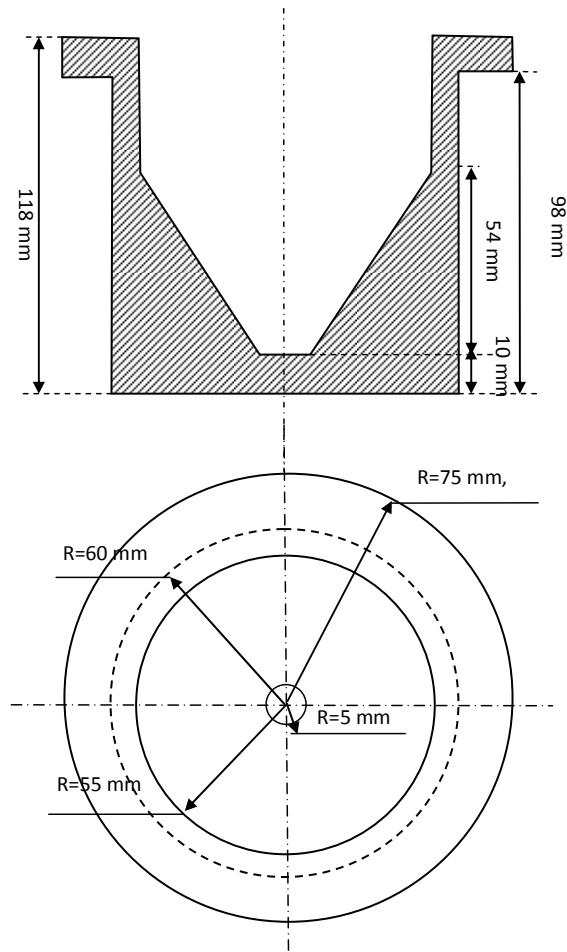
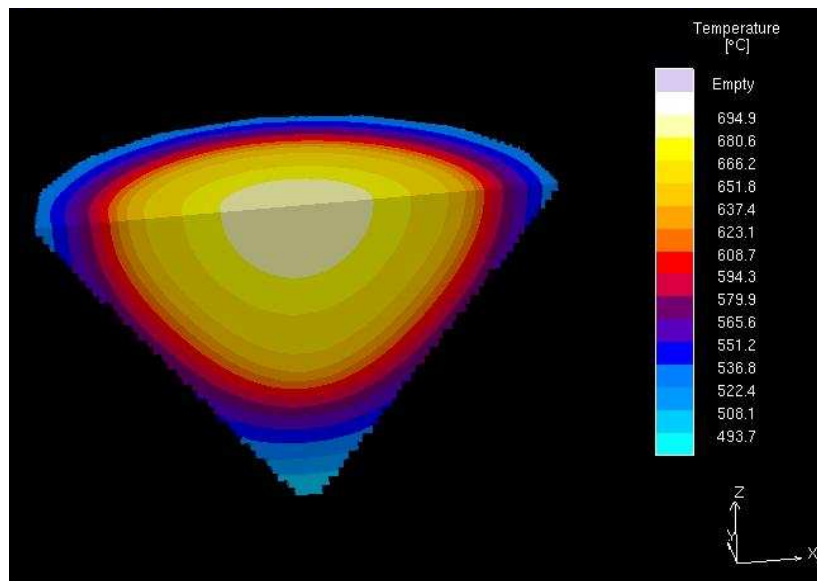
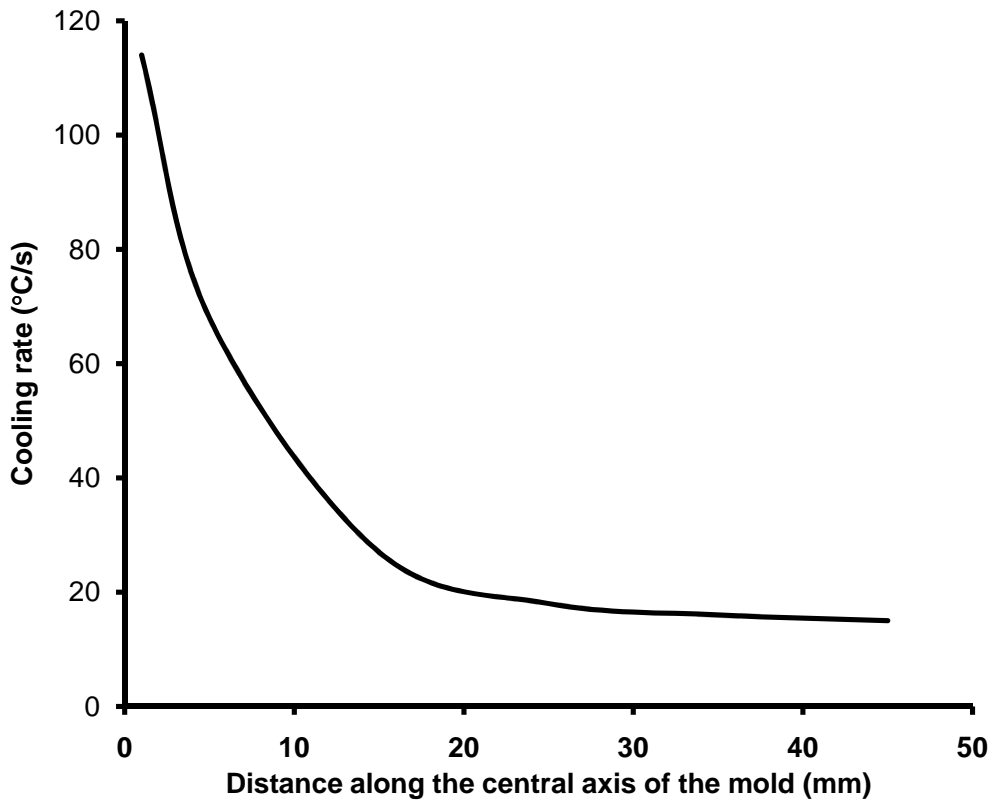


Fig.16. Dimensions of the mold.



(a)



(b)

Fig. 17. Results of the computer simulations (a) temperature distribution in the solidifying ingot, and (b) cooling rate along the central axis of the mold.

The cooling rates were measured along the central axis of the mold. For this purpose, commercially pure aluminum was heated to 1000°C and then cast into the brass mold. Five thermocouples were placed at locations 1mm, 13mm, 25mm, 39mm, and 45mm away from the bottom of the mold. The temperature–time curves were recorded during solidification of the aluminum and plotted as shown in Fig.18. Two regions can be identified in these temperature–time curves. The first starts at the liquidus temperature of the alloy and extends to the end of solidification. The liquidus temperature varies with the composition of the alloys, but is typically in the range 760°C to 820°C[18-23]. The end of solidification may be determined from the temperature–time curves where the end of the plateau indicates the end of the transformation from liquid to solid. The average cooling rate during this stage (δ) is given by Eq.15. Fig.19 shows that δ decreases exponentially from 90°C/s at the bottom of the ingot to 4°C/s at the top.

The second region in the temperature–time curves extends from the end of solidification to room temperature. The average cooling rate during this region is defined as δ' . Unlike δ , δ' changes only slightly with location along the central axis of the mold and is about 3.5°C/s. The first region of temperature–time curves is significant to the precipitation of the primary Al_3M phases, while the second region is not because of the low diffusivity of the transition metals in aluminum at the lower temperatures which are characteristic of the second region [24-28].

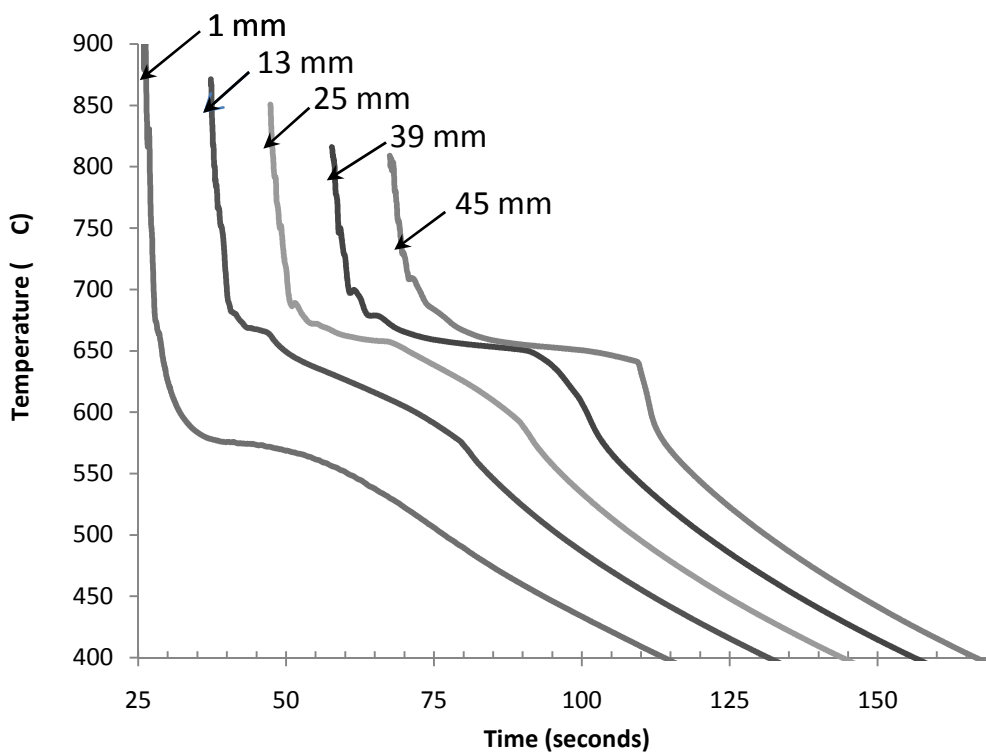


Fig.18. Measured temperature–time curves at different locations along the central axis of the mold.

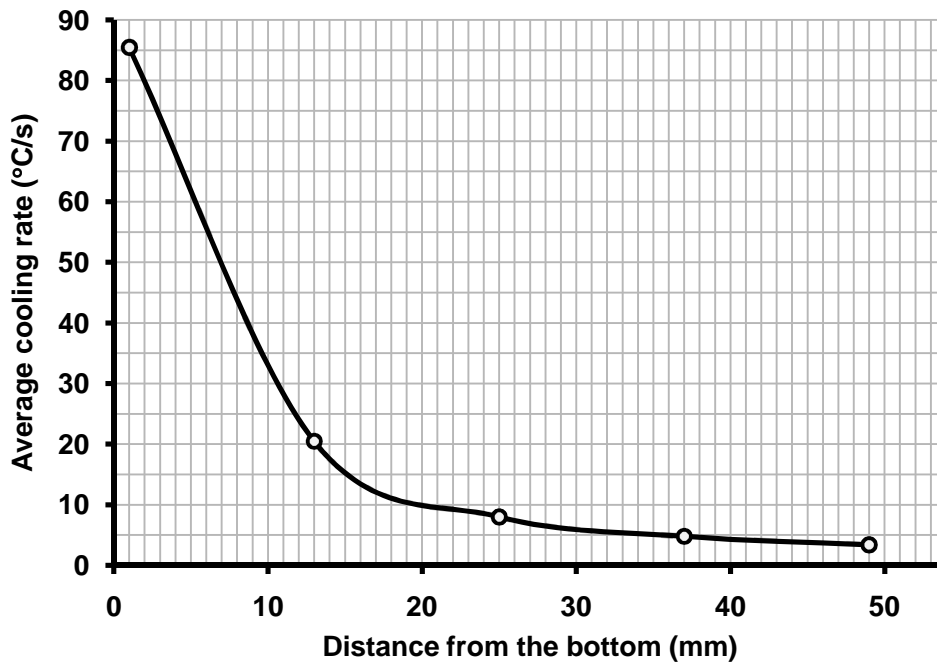


Fig.19. Measured average cooling rates along the central axis of the ingot.

3.2 Design of the Mold used in Measuring Tensile Properties

A water-chilled mold shown schematically in Fig.20 was designed to produce samples for measuring tensile properties. The mold is made of copper to achieve a high cooling rate. Five water channels are drilled in the mold walls to enhance heat extraction from the ingot. The shape of the cast ingot is a disk 0.5 inches in height and 2 inches in diameter, which can then be machine to yield standard tensile test samples. The average cooling rate in an ingot cast in this mold was measured at 3 locations along the thickness of the ingot and was found to be 160°C/s at the top, 60°C/s at the middle, and 28°C/s at bottom.

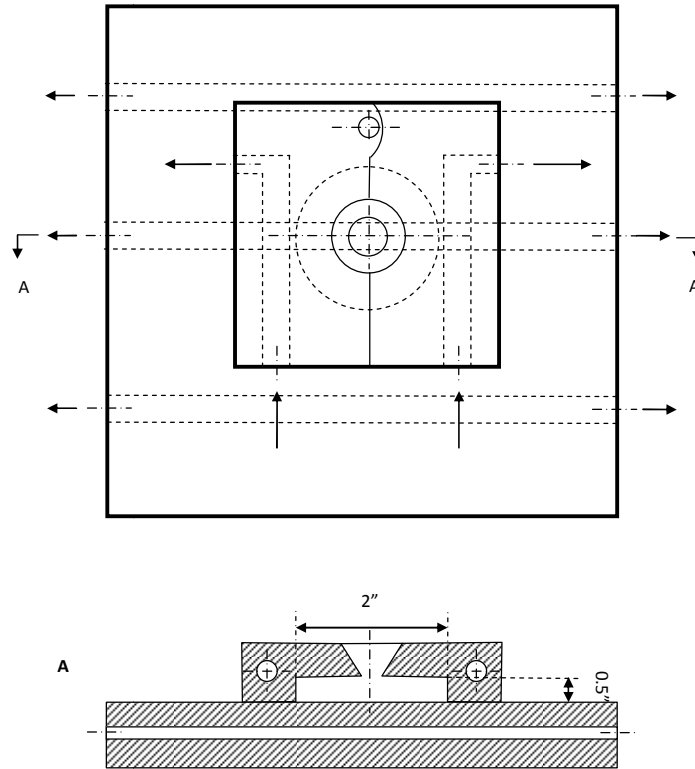


Fig.20. Schematic representation of the water-chilled mold used to cast ingots for tensile property measurements.

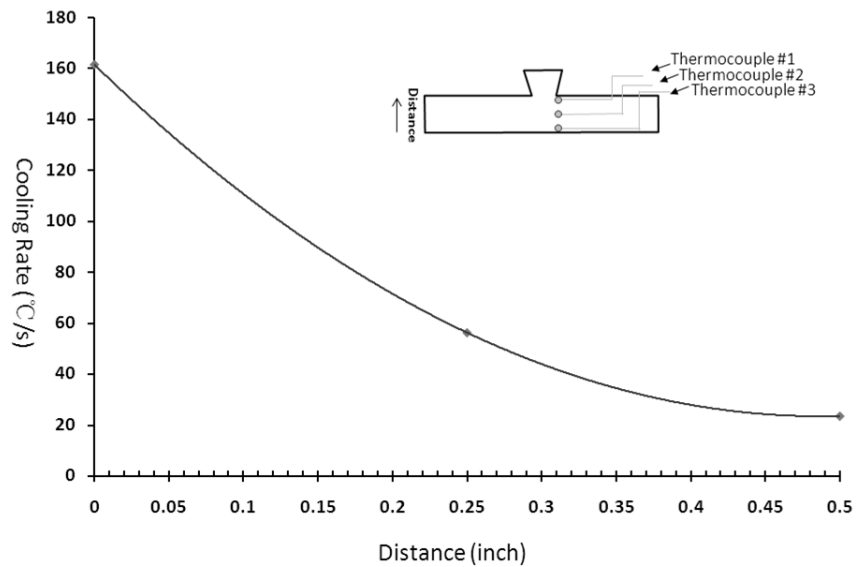


Fig. 21. Measured average cooling rate along the thickness of ingots cast in the water-chilled mold.

3.3 Melt Preparation, Casting, Heat Treatment, and Microstructure Characterization

3.3.1 Melt Preparation and Casting – Alloys with the chemical compositions shown in Table 7 were prepared by induction melting. The alloys were prepared from Al-65V master alloy, 99% purity K₂ZrF₉ salt, 99% purity silicon, and 99.99% purity aluminum. The Al-65V master alloy was pre-ground into ¼ mesh (6.3mm sieve opening).

Table 7. Chemical compositions of the alloys.

Alloy #	Zr (wt.%)	V (wt.%)	Si (wt.%)	Al (wt.%)
1	0.6	0	<0.01	Balance
2	0.1	0.4	<0.01	Balance
3	0.1	0.4	0.2	Balance
4	0.15	0.6	<0.01	Balance
5	0.15	0.6	0.2	Balance

The melting and holding temperature of the alloys was 800°C, which is high enough to ensure that all the zirconium and vanadium melted and dissolved in the aluminum. Alloys 1 to 5 were poured into the cone-shaped brass mold which was immersed in room-temperature water. The pouring temperature was approximately 780°C, which is above the liquidus temperature of the alloys. Alloy 2 was also cast in the water-chilled copper mold in order to produce ingots that were then machined into standard specimens for measuring tensile properties. Alloy 2 was degassed with Ar prior to casting in the water-chilled copper mold.

3.3.2 Establishing the Critical Cooling Rate – In order to establish the critical cooling rate for the Al-0.6Zr and Al-0.4-0.1Zr alloys, samples were extracted from the ingots that were cast in the cone-shaped mold at different locations along the central axis of the ingot so as to represent different cooling rates. The samples were mounted in Bakelite and prepared for metallographic examination using standard procedures. The primary Al₃M phases present in each sample were then observed by a scanning electron microscope (SEM)² and the fraction of the primary phases were counted by means of image analysis software³.

3.3.3 Heat Treatment, Hardness Measurement, and Microstructure Characterization

–Samples were cut from the ingots that were cast in the cone-shaped brass mold from the location where the cooling rate was 85°C/s. These samples were aged in a box furnace according to the schedule shown in Table 8. Evolution of the Al₃Zr and Al₃(Zr_xV_{1-x}) precipitates during aging was monitored by measuring the Vickers microhardness of the specimens, and by transmission electron microscopy⁴. The Vickers microhardness measurements were performed at room temperature with a load of 200g and a dwell time of 5 seconds on samples that were prepared by standard metallographic techniques. For characterizing the samples with conventional transmission electron microscopy, foils were prepared by mechanical grinding sections of the samples to a thickness of about 70µm. Discs with 3 mm diameter were then punched from these foils and thinned to perforation by twin-jet electropolishing at 20V DC with a 25 vol.% solution of nitric acid in methanol at -20°C. Samples for High Resolution TEM were prepared by the focused ion beam (FIB) technique. The samples had an area of approximately 1µm × 3µm and were thinned to 20nm thickness.

² Model JEOL 7000, JEOL USA, Inc., Dearborn Road, Peabody, MA 01960.

³Image-J software.

⁴ JOEL TEM 2010F and JOEL TEM 100CX, JEOL USA, Inc., Dearborn Road, Peabody, MA 01960.

Table 8. Aging schedule.

Alloy	Aging Schedule
1	400°C, and 450°C isothermal aging
2	400°C isothermal aging, 1 hour at 500°C +12 hours at 400°C
3	400°C isothermal aging
4	400°C isothermal aging
5	400°C isothermal aging

3.3.4 Elevated Temperature Tensile Property Measurements- Ingots made from alloy2 by casting in the water-chilled copper mold were machined to produce ASTM standard size tensile specimens for high temperature tensile property measurements. The shape and dimensions of specimens are shown in Fig. 22.

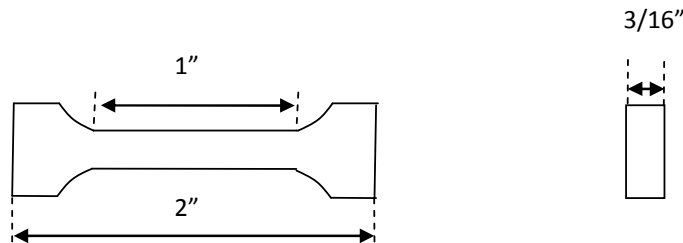


Fig.22. Schematic representation of the specimens used to measure tensile properties.

The elevated temperature tensile property measurements were conducted according to the parameters shown in Table 9. In addition, the tensile properties of commercial purity aluminum were measured at 300°C to provide a base line for comparison.

Table 9.Parameters for measuring the tensile properties of alloy 2.

Aging Parameters	No. of Samples	Test Temperature
1hour at 500°C +12 hours at 400°C	3	300°C
18 hours at 400°C	3	300°C

4. Results and Discussion

4.1 The Effect of Cooling Rate on the Volume Percent of the Primary Al₃M Phase

4.1.1 The Binary Al-Zr System

The Primary Al₃Zr phase was detected by SEM in the Back Scattered Imaging Mode. Because the atomic number of zirconium is much higher than that of aluminum, the primary phase can be clearly distinguished by the Z-contrast in Back Scattered Imaging Mode. Fig.23 shows the typical morphologies of the primary Al₃Zr phase. The volume of an individual particle of primary Al₃Zr phase is estimated to be around 7μm. As Fig.24 shows, more of the primary phase precipitate formed in samples cooled at different cooling rates. While SEM pictures cannot be used to give accurate calculations of the volume fraction of these irregularly-shaped precipitates because of their lack of 3-D information, the average area fraction of the primary phase ($f_{Al_3M}(\delta)$ ($M = Zr, V, el.$)) as a function of cooling rate (δ) can be calculated from SEM pictures; and it is given by

$$f_{Al_3M}(\delta) = \frac{e_{Al_3M}(\delta)}{e_{Al_3M}(\delta \rightarrow 0^\circ C/s)} \quad (16)$$

In Eq. (16), $e_{Al_3M}(\delta)$ is the area fraction of the primary phase in samples cooled at cooling rate δ ; and $e_{Al_3M}(\delta \rightarrow 0^\circ C/s)$ is the area fraction of primary phase in samples solidified extremely slowly - i.e., samples in which nearly all the transition elements precipitated as primary phase. Considering that the driving force to precipitate the primary phase is very high in the Al-0.6Zr system, it is reasonable to assume that nearly all the zirconium precipitates as primary Al₃Zr when the cooling rate is 10°C/s. Hence, the average area fraction of the primary phase in the case of Al₃Zr can be given by

$$f_{Al_3Zr}(\delta) = \frac{e_{Al_3Zr}(\delta)}{e_{Al_3Zr}(\delta=10^\circ C/s)} \quad (17)$$

Fig.25 shows the variation of the area fraction of primary Al₃Zr with cooling rate. The area fraction of primary Al₃Zr is nearly zero at an average cooling rate of 95°C/s and a large amount of primary Al₃Zr is present at lower average cooling rates, which indicates that Al-0.6Zr alloy is a supersaturated solid solution only when it is quenched with a cooling rate that is higher than 95°C/s.

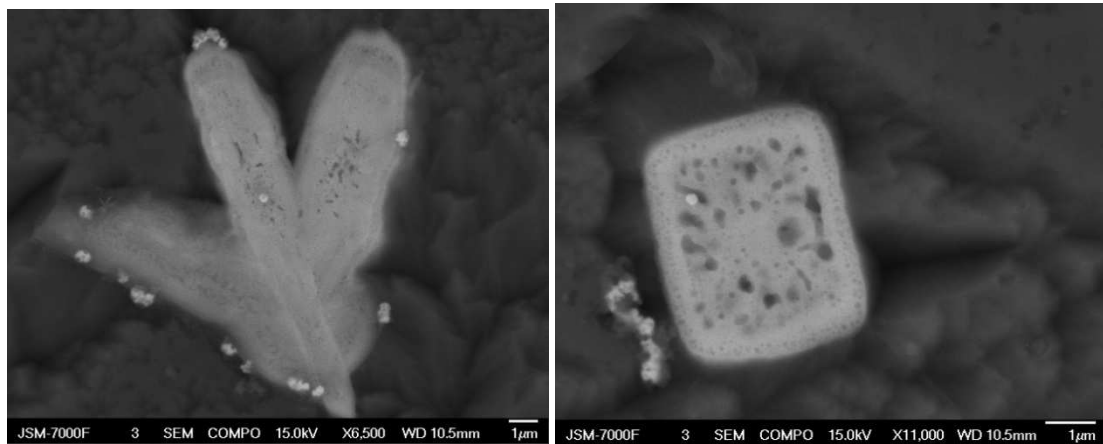
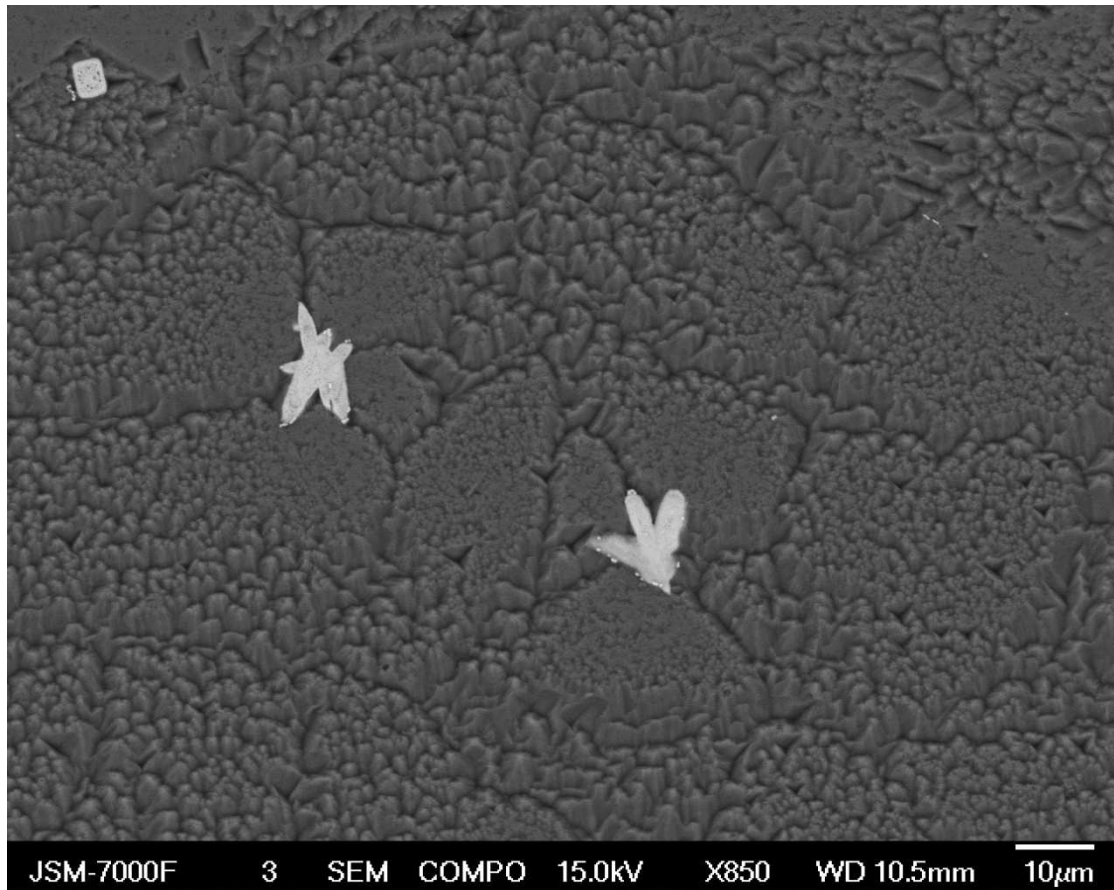
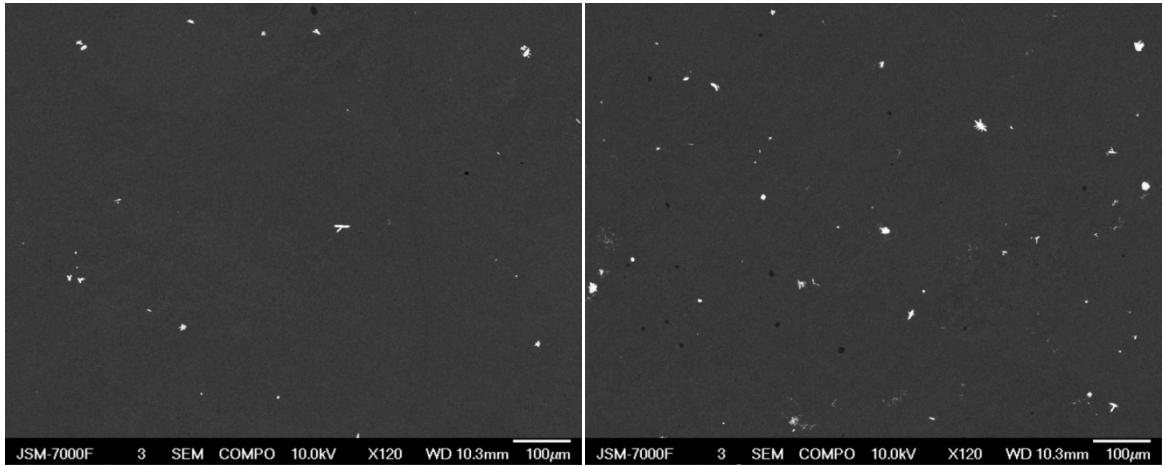
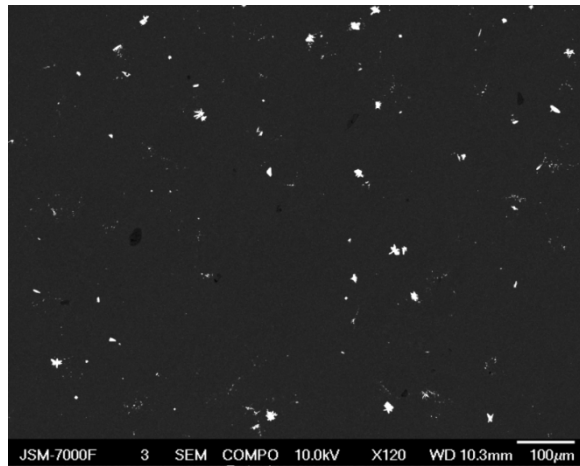


Fig.23. Morphologies of the primary Al_3Zr phase in Al-Zr alloys.



(a)

(b)



(c)

Fig.24. Backscattered SEM images of the Al_3Zr primary phase in samples cooled with different cooling rates. (a) 80°C/s , (b) 45°C/s , and (c) 10°C/s .

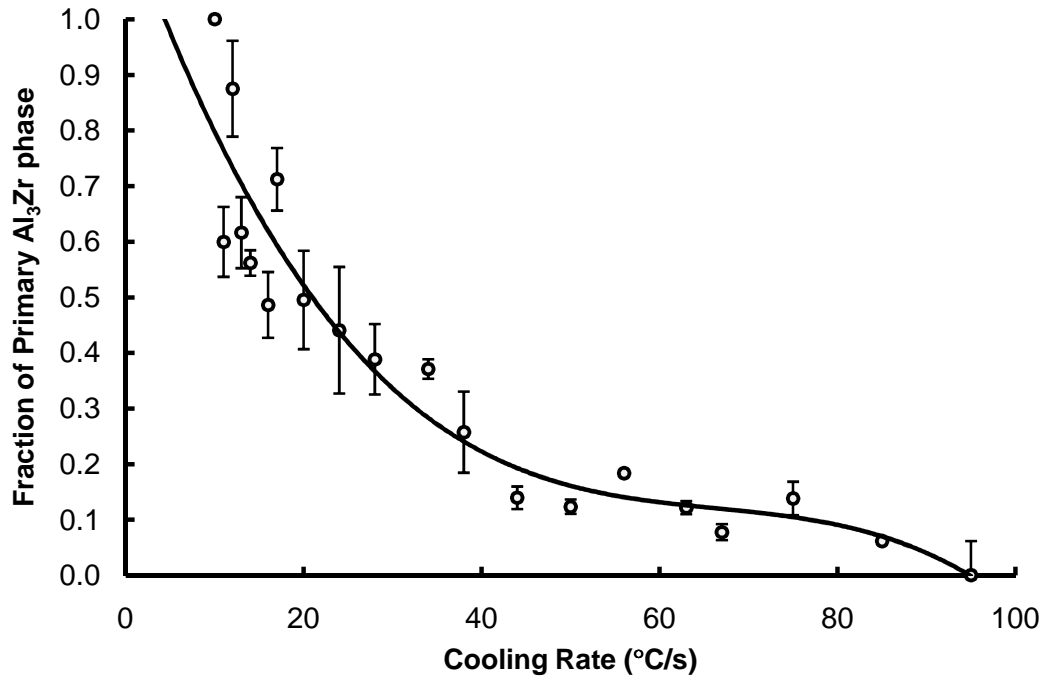
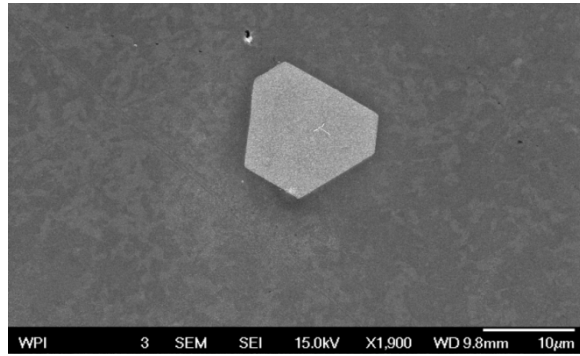


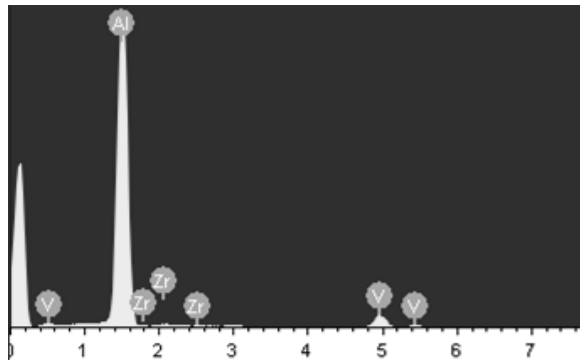
Fig.25. Variation of the area fraction of primary Al₃Zr with cooling rate.

4.1.2 The Ternary Al-Zr-V System

The same method used with the binary Al-Zr system is applied to analyze Al-0.4V-0.1Zr, Al-0.4V-0.1Zr-0.2Si, Al-0.6V-0.15Zr and Al-0.6V-0.15Zr-0.2Si alloys. The EDS and SEM image shown in Fig.26 indicate that the primary phase that forms in ternary Al-Zr-V alloys is Al₃(Zr,V) co-precipitate with a polygonal morphology. Fig. 27 shows the variation of the area fraction of primary Al₃(Zr,V) with cooling rate. The critical cooling rate of the Al-0.4V-0.1Zr alloy is 35°C/s, which is lower than that of the Al-0.6Zr alloy. Moreover, the combined mole fraction of vanadium and zirconium in the Al-0.4V-0.1Zr alloy is higher than the mole fraction of zirconium in the Al-0.6Zr alloy. Therefore it can be deduced that substituting vanadium for zirconium suppresses the formation of Al₃M primary precipitates. However, when the concentration of vanadium is 0.6 wt%, a higher cooling rate (> 85°C/s) is necessary to suppress formation of the primary phase. Also, it can be seen from Fig. 26 that adding Si to these alloys accelerates precipitation of the primary phase.

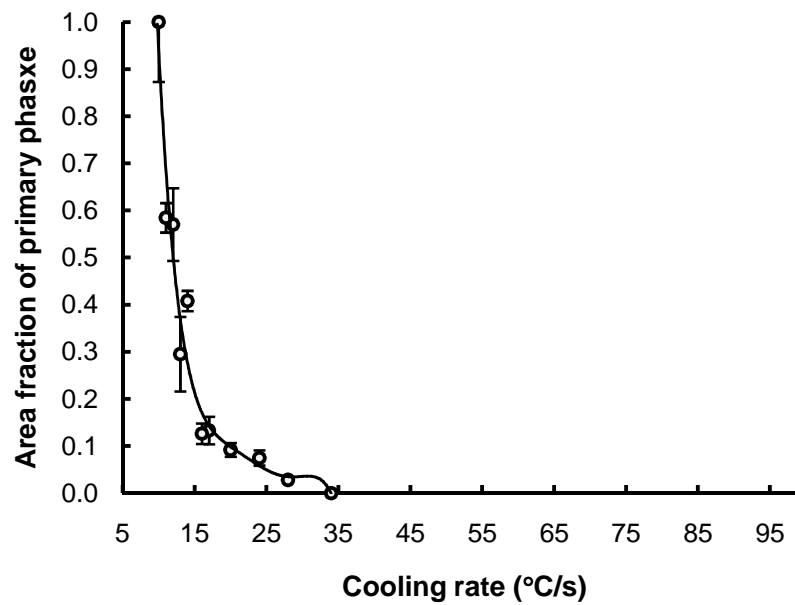


(a)

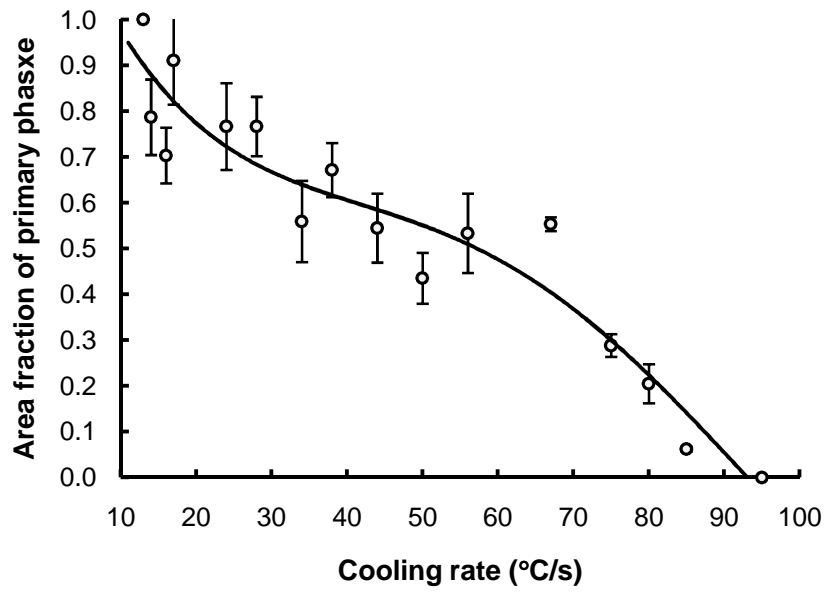


(b)

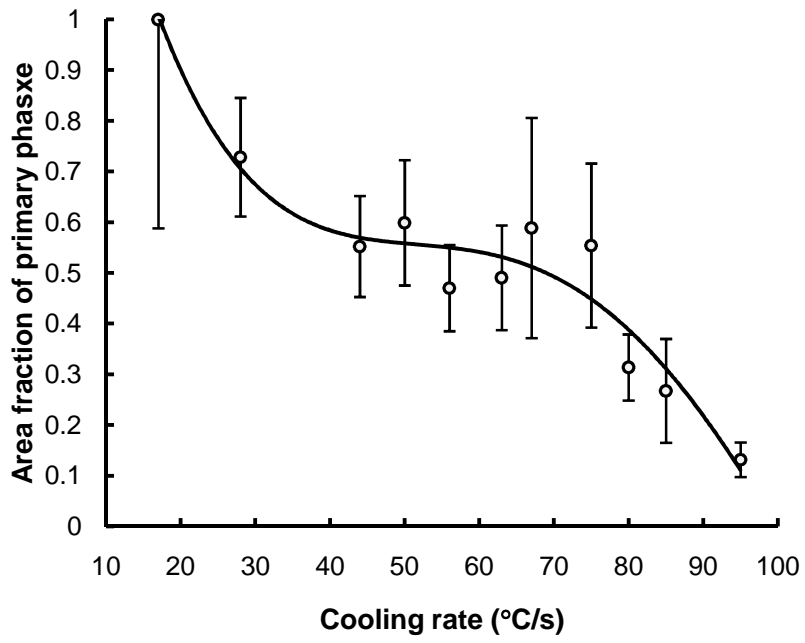
Fig. 26. (a) SEM image of a primary particle in Al-0.4V-0.1Zr alloy, and (b)EDS of the particle shown in (a).



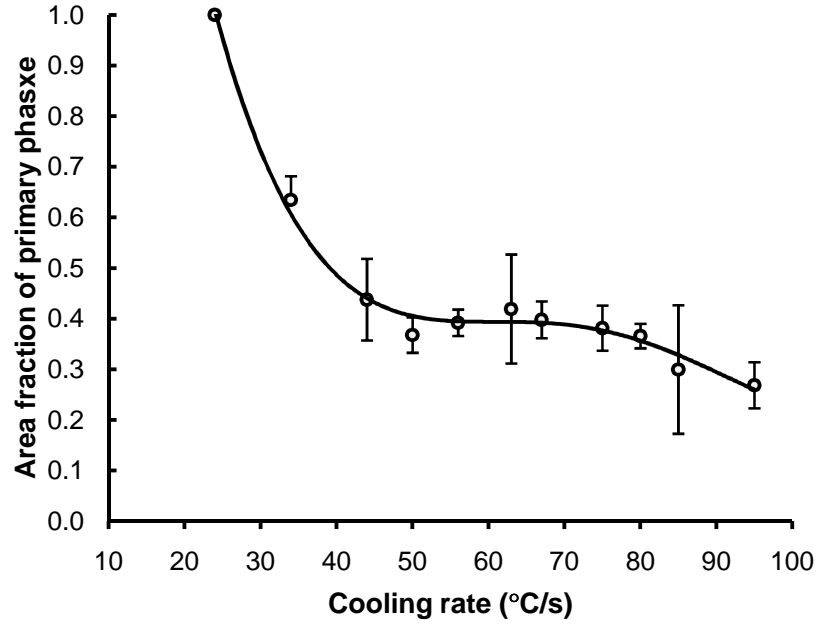
(a)



(b)



(c)



(d)

Fig.27. Variation of the area fraction of primary $\text{Al}_3(\text{Zr},\text{V})$ with cooling rate in (a) Al-0.4V-0.1Zr alloy, (b) Al-0.4V-0.1Zr-0.2Si alloy, (c) Al-0.6V-0.15Zr alloy, and (d) Al-0.6V-0.15Zr-0.2Si alloy.

As the Volmer-Weber theory ⁽⁵⁹⁾ predicts, nucleation rate (N_{hom}) is related to undercooling (ΔT) by

$$N_{hom} = f_0 C_0 \exp\left(-\frac{A}{(\Delta T)^2}\right) \quad (18)$$

where f_0 is a complex function that depends on the vibration frequency of the atoms, the activation energy for diffusion in the liquid, and the average surface area of the critical nucleus. The value of f_0 is estimated to be $\sim 10^{11}$, C_0 is typically considered a constant and its value is $\sim 10^{29}$ atoms/ m^3 , and $A = \frac{16\pi\sigma_{SL}^3 T_m^2}{3L_v^2}$.

As Eq.(18) indicates, higher undercooling results in faster nucleation rate. The slope of the liquidus in the Al-V binary system at the Al-rich corner is gentler than that of the Al-Zr binary system; and the difference between the liquidus and solidus temperatures of Al-0.6Zr (0.18 at.% Zr) is 159°C . For the Al-0.4V (0.18 at.% V), it is only 69°C . Therefore the substitution of vanadium for zirconium lowers the critical cooling rate needed to suppress formation of the primary phases.

4.2. Isothermal Heat Treatment of Binary Al-Zr and Ternary Al-Zr-V Alloys

4.2.1 The Binary Al-Zr Alloy

The variation in Vickers microhardness of an Al-0.6Zr sample that has been quenched at 90°C/s is shown in Fig.28. As mentioned earlier, with a cooling rate of 90°C/s , the Al-0.6Zr alloy is a supersaturated solid solution. Fig.28 shows that this supersaturated solid solution is age-hardenable at 400°C and 450°C , which is in agreement with other works ⁽⁶¹⁾. The Al-0.6Zr supersaturated solid solution reaches its peak hardness of 41 HV_{200} after aging for 12 hours at 450°C , after that time, the hardness begins to decrease. When aged at 400°C , the Vickers hardness of the alloy continues to increase steadily with time up to 24 hours, at which time aging was discontinued.

Fig. 29 is a composite plot that shows the hardness of the Al-0.6Zr alloy as a function of cooling rate. As mentioned earlier, the lower cooling rates result in higher fractions of the primary phase which does not contribute to precipitation hardening. When the cooling rate is about 10°C/s , the hardness of the alloy is 27 HV_{200} , and the alloy does not respond to aging, which implies that at this cooling rate nearly all the zirconium content of the alloy is in the primary phase.

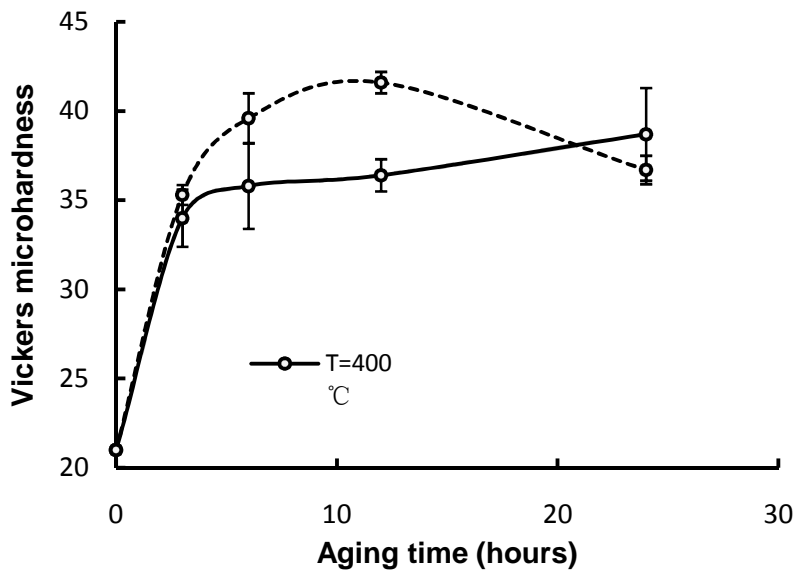


Fig.28. Variation of the hardness of optimally-quenched Al₃Zr alloy with aging temperature and time.

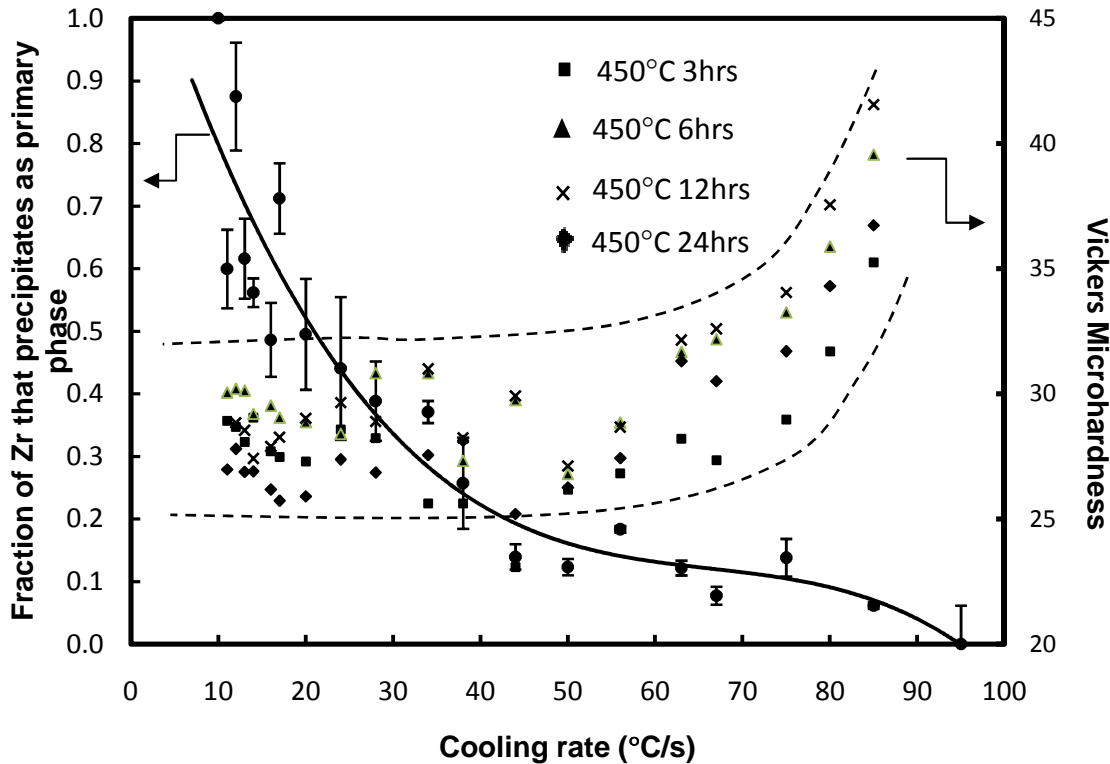


Fig.29. Variation of the hardness of Al_3Zr alloy cooling rate, aging temperature and time.

4.2.2 The Ternary Al-Zr-V Alloys

The Vickers microhardness of alloys 2, 3, and 5 is shown in Fig. 30. All these isothermally aged alloys were quenched with a cooling rate of 90°C/s . As seen in Fig. 30, the maximum microhardness of Al-0.4V-0.1Zr is 39 HV_{200} and it is achieved in samples aged at 400°C for 18 hours. The peak hardness of $\text{Al-0.4V-0.1Zr-0.2Si}$ alloy is 41 HV_{200} and is achieved by aging at 400°C for only 12 hours. Despite that only about 80% of the vanadium and zirconium used to make the $\text{Al-0.6V-0.15Zr-0.2Si}$ alloy were dissolved into the aluminum to form a supersaturated solid solution when the alloy was quenched at 90°C/s , this alloy exhibited remarkably high microhardness when it was aged at 400°C for 24 hours (60 HV_{200}) and the hardness remained constant after holding the alloy for 36 hours, upon which time the experiment was stopped.

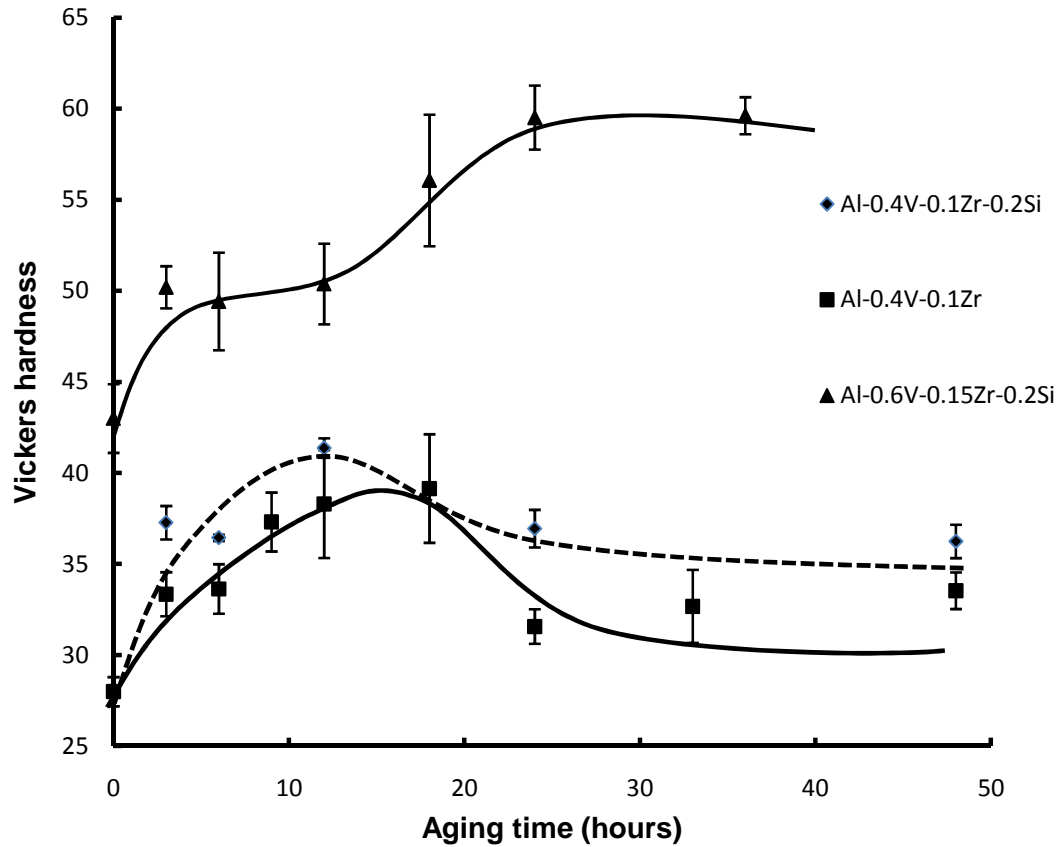


Fig.30. Variation of the hardness of optimally-quenched Al-0.4V-0.1Zr, Al-0.4V-0.1Zr-0.2Si, and Al-0.6V-0.15Zr-0.2Si alloys with aging temperature and time.

4.2.3 Thermal Stability of Al-0.4V-0.1Zr Alloy

A sample of alloy Al-0.4V-0.1Zr that was optimally-quenched and aged at 400°C for 12 hours was soaked at 300°C in order to assess the thermal stability of the Al₃(Zr,V) precipitates. The result is shown in Fig.27 as a plot of Vickers hardness vs. time at 300°C. It is clear that the Vickers hardness remain constant at 39 HV₂₀₀ up to 100 hours, at which time the experiment was discontinued. Alloy Al-0.4V-0.1Zr is stable and may be used in applications that require thermal stability at temperatures up to 300°C.

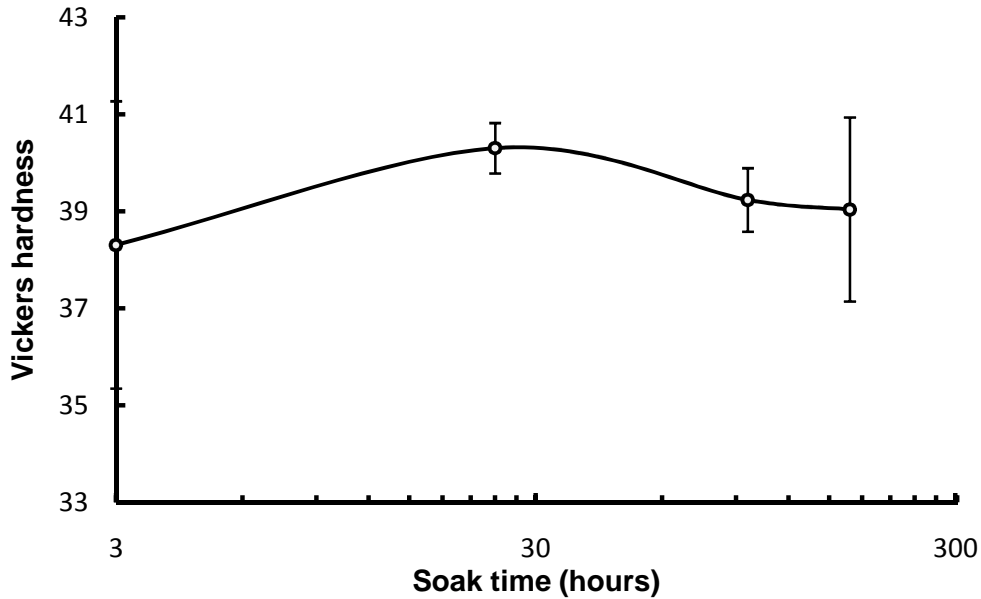


Fig.31. Variation of the Vickers hardness of alloy Al-0.4V-0.1Zr (optimally-quenched and aged at 400°C for 12 hours)with exposure time to 300°C temperature.

4.3 Morphology and Crystal Structure of The $Al_3(Zr,V)$ Precipitates

Figs. 32 and 33 show TEM and HRTEM micrographs of the $Al_3(Zr,V)$ precipitates. The image in Fig. 32 is from a sample of alloy Al-0.4V-0.1Zr that was aged for 1 hour at 500°C followed by 12 hours at 400°C. The mean radius of the precipitate particles is about 7nm. Fig. 33 is from a sample of alloy Al-0.6V-0.15Zr-0.2Si that was aged for 12 hours at 400°C. The mean radius of the $Al_3(Zr,V)$ precipitate particles is about 1nm. The $Al_3(Zr,V)$ precipitates are uniformly dispersed in both alloys. However, the radius of the precipitates in Al-0.4V-0.1Zr is much larger than that in Al-0.6V-0.15Zr-0.2Si because the Al-0.4V-0.1Zr alloy was pre-age at 500°C, which accelerated coarsening of the precipitates. In both the Al-0.6V-0.15Zr-0.2Si alloy and the Al-0.4V-0.1Zr alloy the precipitate particles are coherent with the aluminum matrix. In producing the image in Fig. 32, the sample was tilted to two beam condition; under this imaging condition, coherent phases exhibit the characteristic Ashby-Brown strain contrast. Fig. 32 shows that not only are the precipitates fully coherent with the aluminum matrix, but they have matching lattice parameters.

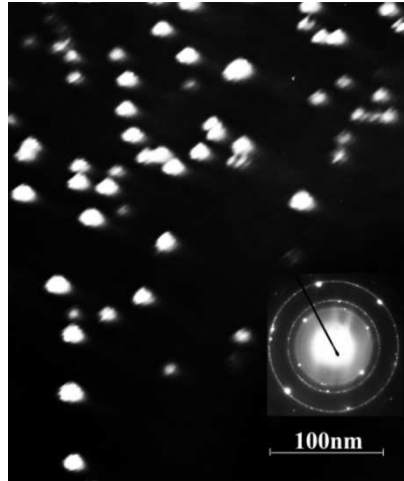


Fig. 32. TEM pictures of L1₂-structure of Al₃(Zr,V) precipitates in Al-0.4V-0.1Zr alloy. The sample was tilted to the [110] zone axis.

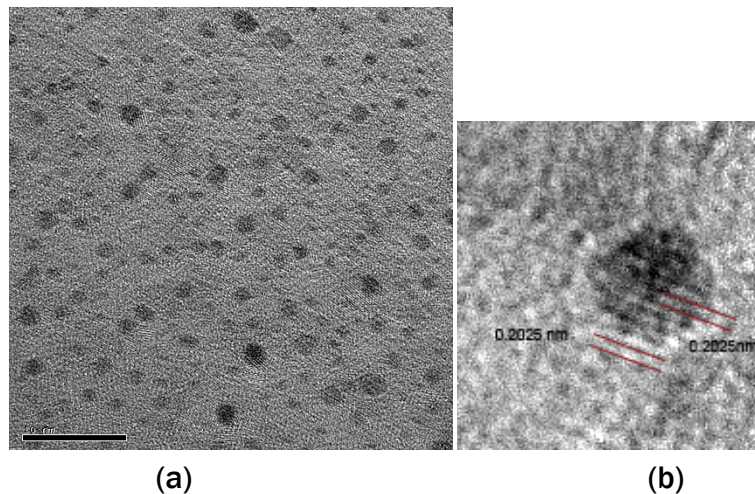


Fig.33. (a)HRTEM image of Al-0.6V-0.15Zr-0.2Si alloy. (b) higher magnification of the image in (a)

The hardness of heat-treated Al-Zr alloys is negligible if the concentration of zirconium in the alloy is below 0.4 wt.%. This is attributed to the limited volume fraction of L1₂ precipitates [68] that form with such low concentration of zirconium. However, as Fig.30 shows, the hardness of Al-Zr-V alloys increases upon aging at 400°C. The hardness of aged Al-0.6V-0.15Zr-0.2S alloy is 60 HV₂₀₀, which is almost three times as high as the hardness of the heat-treated Al-0.27Zr alloy [67]. The substitution of vanadium for zirconium increases the density of the L1₂ precipitates, and therefore, as Ashby-Orowan theory predicts, it increases the hardness of the alloy.

The TEM images in Figs. 32 and 33 show a high volume density of L1₂ precipitates in the matrix of Al-V-Zr alloys after proper heat treatment. Also, Fig. 33 shows that the misfit between the Al₃(Zr,V) precipitate particles and the α-Al matrix is eliminated when the V:Zr atom fraction ratio in the precipitate is 0.875 (the Al₃(Zr,V) precipitates in the Al-0.6V-0.15Zr-0.2Si alloy are fully coherent with the matrix); for this reason alloy Al-0.4V-0.1Zr is thermally stable at temperatures up to 300°C.

As Fig. 30 shows, adding Si to Al-V-Zr alloys increases the critical cooling rate needed to suppress formation of the primary phase. It has been suggested [66] that clusters of a primary silicon phase which form during solidification act as heterogeneous nucleation sites for the Al₃M primary phases, and thus A in Eq. (19) becomes

$$A_{Het} = \frac{16\pi\sigma_{SL}^3 T_m^2}{3L_v^2} * f(\theta) \quad (19)$$

where $f(\theta)$ is a function of the contact angle between the liquid and the silicon clusters. The value of $f(\theta)$ is between 0 and 1. Therefore, the critical cooling rate is increased with the addition of Si. Also, the silicon clusters are effective in precipitating the Al₃(Zr,V) L1₂ particles [64 -65]. This is clear from Fig. 26 which shows that the hardness of the Al-0.4V-0.1Zr-0.2Si alloy reaches its peak 6 hours earlier than that of Al-0.4V-0.1Zr alloy.

4.4 Elevated Temperature Tensile Properties

Fig. 34 shows the typical strain-stress curve of the heat-treated alloy 2 and also pure aluminum at 300°C. The yield strength of the heat-treated Al-0.4V-0.1Zr alloy is 300% higher than that of pure aluminum due to precipitation hardening. And the high temperature yield strength is dependent on the aging schedule (Fig. 35). Pre-aging the alloy at 500°C causes the precipitates to coarsen, and as the Ashby-Orowan equation suggests, the yield strength drops as the mean radius of the precipitates increase.

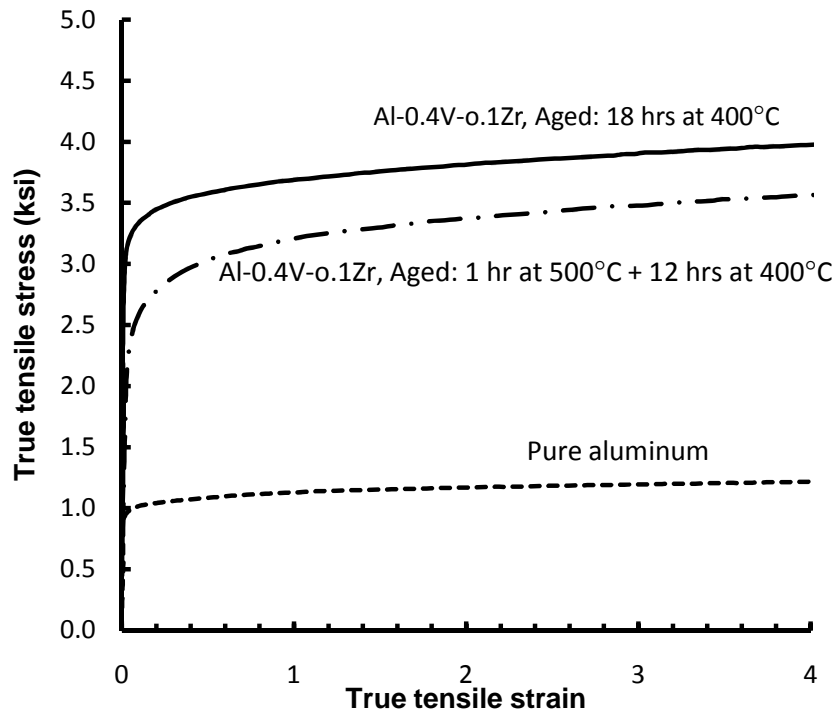


Fig.34. Typical stress-strain curves of Al-0.4V-0.1Zr alloys and pure aluminum at 300°C.

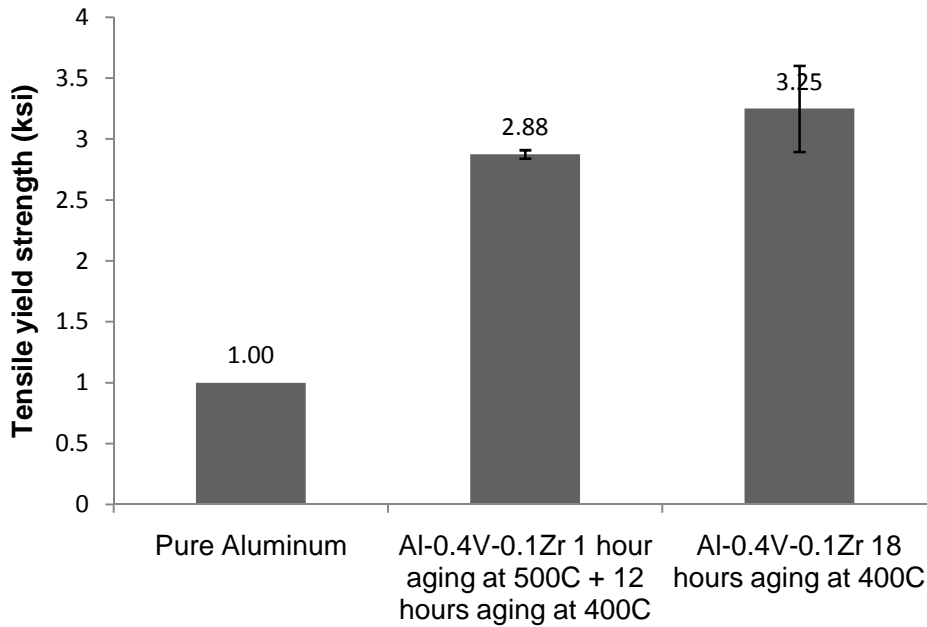


Fig.35. Average yield strength of aged Al-0.4V-0.1Zr and pure aluminum at 300°C.

5. Conclusions

1. Substituting vanadium for zirconium in aluminum-zirconium alloys significantly decreases the critical cooling rate of the alloy. The critical cooling rate of Al-0.6Zr and Al-0.4V-0.1Zr alloys are measured to be 90°C/s and 35°C/s respectively. This is an important finding since these thermally stable alloys can now be used to manufacture components by high pressure die casting.
2. It has been shown that vanadium co-precipitates with zirconium and aluminum upon proper aging and forms spherical, nanosize particles that have the L1₂ crystal structure, and that are fully coherent with the α -aluminum matrix.
3. The Al₃(Zr,V) precipitates are thermally stable up to 300°C and they add about 2 Ksi to the yield strength of pure aluminum at 300°C.

6. References

- (1) Wilm, A., Metallurgie, vol.8, pp225 (1911).
- (2) Merica, P.D., Waltenberg, R.G., and Scott, H., Sci.Paper, pp347 (1919).
- (3) Guninier, A., Compt. Rend., vol.206, pp1641 (1938).
- (4) Kelly, A., Nicholson, R.B., Progr. Mater. Sci., vol.10,pp151(1963).
- (5) Mott,N.F., Nabarro,F.R.N., Proc. Phys. Soc., vol.52,pp86 (1940).
- (6) Orowan, W., 'Internal stress in metals and alloys', p.451, The Institute of Metals,London(1984).
- (7) Ashby, M.F., Oxide Dispersion Strengthening, p.143, Gordon and Breach, New York (1958).
- (8) Mott, N.F., Nabarro, F.R.N., The Physical Society (1948).
- (9) Zedalis, M.S., Fine,M.E., Scripta Metall., vol.19, pp647 (1985).
- (10) Hirsch,P.B., Kelly,A., Phil. Mag., vol.12, pp220 (1965).
- (11) Gerold,V., Hartmann,K., Trans. Japan. Inst. Metals, vol.9,pp509 (1968).
- (12) Lifshitz,I.M., Slyozov, V.V., J. Phys. Chem. Solids,vol.19 pp35 (1961).
- (13) Wanger,C., Z. Elektrochemie,vol.65 pp581 (1961).
- (14) Röhrle, M. D., Pistons for Internal Combustion Engines, Verlag Moderne Industrie, (1995).
- (15) Okamoto,H., Phase Diagrams of Dilute Binary Alloys, ASM Internatioal, Materials Park (2002)
- (16) Murray, J.L., Peruzzi,A., Abriata,J.P., J. Phase Equil. Vol.13,pp277(1992).
- (17) Fine, M.E., Metall. Trans. A, vol.6,pp625(1975).
- (18) Okamoto,H., Phase Diagrams of Dilute Binary Alloys ASM International, Materials Park (2002).
- (19) Murray,J.L., J. Phase Equil.,vol.19, pp380 (1998).
- (20) Massalski, T.B., Binary Alloy Phase Diagram, Vol.1., 2nd ed. ASM International, Materials Park (1990).
- (21) Liang, W.W., CALPHAD,vol.7, pp13 (1983).
- (22) Murrary, J.L., Peruzzi,A., Abriata,J.P., J. Phase Equil.,vol.13,pp277 (1992).
- (23) Murray, J.L., McAlister,A.J., Kahan,D.J., J. Phase Equil.,vol.19,pp376 (1998).
- (24) Fujikawa, S.I., Def. Diff. Forum, vol.116, pp143 (1997).
- (25) Bergner,D., van Chi,N., Wissenschaftliche Zeitschrift der padagogischen Hochschule,vol.15, (1977)

- (26) Marumo, T., Fujikawa, S., Hirano, K., J. Japan Inst. Light Metals, vol.23, pp17 (1973).
- (27) Fujikawa, S.I., J. Japan Inst. Light Metals, vol.46, pp22 (1996).
- (28) Rummel, G., Zumkley, T., Eggersman, M., Freitag, K., Mehrer, H., Z. Metallkd. Vol.86, pp122 (1995).
- (29) Murphy, J.B., Acta. Metall., vol.9 pp563 (1961).
- (30) Beerwald, A., Z. Elektrochem., vol.45, pp789 (1939).
- (31) Marquis, E.A., Seidman, D.N., Acta. Mater., vol.49, pp1909 (2001).
- (32) Ryum, N., Acta. Metall., vol.17, pp269 (1969).
- (33) Zedalis, M.S., Fine, M.E., Metall. Trans. A, vol.17, pp2187 (1986).
- (34) Keith E. Knipling, David C. Dunand, Acta. Mater., vol.58, pp1182 (2008).
- (35) Christian B. Fuller, David N. Seidman, David C. Dunand, Acta. Mater., vol.51, pp4803 (2003).
- (36) Belov, N.A., Alabin, A.N., Eskin, D.G., J. Mater. Sci., vol.41, pp5890 (2006).
- (37) Keith E. Knipling, Richard A. Karnesky, Acta. Mater., vol.58, pp5184 (2010).
- (38) Lefebvre, W., Danoix, F., J. Alloys and Compounds, vol.470, pp107 (2009).
- (39) Senkov, O.N., Shagiev, M.R., Acta. Mater., vol.56, pp3723 (2008).
- (40) Tolley, A., Radmilovic, V., Scripta Mater., vol.52, pp621 (2005).
- (41) Christian B. Fuller, Joanne, L., Muarry, Acta. Mater., vol.53 pp5401 (2005).
- (42) Forbord, B., Lefebvre, W., Scripta Mater., vol.51, pp333 (2004).
- (43) Radmilovic, V., Tolley, A., Scripta Mater., vol.58, pp529 (2008).
- (44) Marsha E. van Dalen, J. Mater. Sci., vol.41, pp7814 (2006).
- (45) Keith E. Knipling, David C. Dunand, Acta. Mater., vol.56, pp114 (2008).
- (46) Hallem, H., Lefebvre, W., Mater. Sci. and Eng. A, vol.421, pp154 (2006).
- (47) Gang Du, Jingwei Deng, Scripta Mater., vol.61, pp532 (2009).
- (48) Matthew E. Krug, Alexandra Werber, and Dunand, D.C., Acta. Mater., vol.58 pp134 (2010).
- (49) Wen, S.P., Gao, K.Y., Scripta Mater., In Press.
- (50) Chun-Huei Tsau, Yen-Cheng Chen, Mater. Phy. and Chem., vol.73, pp111 (2002).
- (51) Won-Wook Park, Mater. and Design., vol.17, pp85 (1996).
- (52) Chen, Y.C., Fine, M.E., Acta. Metall., vol.38, pp771 (1990).
- (53) srinivasan, S., Desch, P.B., Schwarz, R.B., Scripta Metall. Mater., vol.25, pp2513 (1991).
- (54) Nes, E., Acta Metall., vol.20 pp499 (1972).

- (55) Vecchio, K.S., Williams, D.B., *Acta Metall.*, vol.35, pp2969 (1987).
- (56) Xu, J.H., Freeman, A.J., *J. Mater. Res.*, vol.6, pp1188 (1991).
- (57) S.K. das, J.H. Westbrook, R.L. Fleischer (Eds.) *Intermetallic Compounds, Principles and Practice*, vol.2, pp175, John Wiley & Sons (1994).
- (58) Turnbull, D., Fisher, J.C., *J. Chem. Phys.*, vol.17, pp71 (1949).
- (59) Ryum, N., *Acta Metall.*, vol.17, pp269 (1969).
- (60) Keith. E. Knippling, David. C. Dunand, *Metall. and Mater. Trans. A*, vol.38 pp25532 (2007).
- (61) Nes, E., Billdal, H., *Acta Metall.*, vol.25, pp1031 (1977).
- (62) Chen, Y.C., Fine, M.E., and Weertman, J.R., *Acta. Meter.*, vol.38, pp771 (1990).
- (63) Chen, Y.C., Fine, M.E., and Weertman, J.R., *Scripta Metall.*, vol.21 pp1003 (1987).
- (64) Hori, S., Saji, S., and Higaki, Y., *J. Japan Inst. Light Metals*, vol.25, pp247 (1975).
- (65) Takeshi Ikeda, Takashi Tachikawa and Masakio Ikeda., *Mater. Trans., JIM*, vol.38, pp413 (1997).
- (66) Murray, J.L., McAlister, A.J., *Bulletin of Alloy Phase Diagram*, vol.5, pp74 (1984).
- (67) Wen, S.P., Gao, K.Y., Li, Y., Huang, H., and Nie, Z.R., *Scripta Materialia*, (2011), Inpress.
- (68) Belov, N.A., Alabin, A.N., Eskin, D.G., Istomin Kastrovskii, V.V., *J. Mater. Sci.* vol.42, pp5890 (2006).